

Fall 2013

Development of analytical and experimental tools for magnetic pulse welding

Ethan Hunter Thibaudeau
University of New Hampshire, Durham

Follow this and additional works at: <https://scholars.unh.edu/thesis>

Recommended Citation

Thibaudeau, Ethan Hunter, "Development of analytical and experimental tools for magnetic pulse welding" (2013). *Master's Theses and Capstones*. 826.
<https://scholars.unh.edu/thesis/826>

This Thesis is brought to you for free and open access by the Student Scholarship at University of New Hampshire Scholars' Repository. It has been accepted for inclusion in Master's Theses and Capstones by an authorized administrator of University of New Hampshire Scholars' Repository. For more information, please contact nicole.hentz@unh.edu.

**DEVELOPMENT OF ANALYTICAL AND EXPERIMENTAL TOOLS FOR
MAGNETIC PULSE WELDING**

BY

ETHAN HUNTER THIBAudeau
B.S., University of New Hampshire, 2011

Submitted to the University of New Hampshire

In Partial Fulfillment of

The Requirements for the Degree of

Master of Science

in

Mechanical Engineering

September, 2013

UMI Number: 1524460

All rights reserved

INFORMATION TO ALL USERS

The quality of this reproduction is dependent upon the quality of the copy submitted.

In the unlikely event that the author did not send a complete manuscript and there are missing pages, these will be noted. Also, if material had to be removed, a note will indicate the deletion.



UMI 1524460

Published by ProQuest LLC 2013. Copyright in the Dissertation held by the Author.

Microform Edition © ProQuest LLC.

All rights reserved. This work is protected against unauthorized copying under Title 17, United States Code.

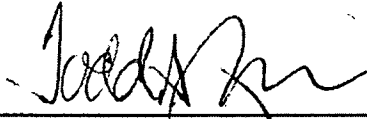


ProQuest LLC
789 East Eisenhower Parkway
P.O. Box 1346
Ann Arbor, MI 48106-1346

This thesis has been examined and approved.



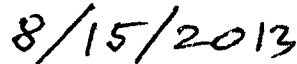
Thesis Director, Dr. Brad Lee Kinsey,
Professor and Chair of Mechanical Engineering



Dr. Todd Gross,
Professor of Mechanical Engineering



Dr. Marko Knezevic,
Assistant Professor of Mechanical Engineering



Date

DEDICATION

To Mémère for inspiring me to be inquisitive from an early age,
And to my parents and grandparents for their loving support and encouragement.

AKNOWLEDGEMENTS

Funding from the U.S. National Science Foundation (CMMI-0928319) is gratefully acknowledged.

I would like to thank Dr. Brad Lee Kinsey for his constant guidance and positive support. It was a privilege to work with him on such an interesting project that involved both theoretical and experimental work.

I would also like to acknowledge Reid VanBenthysen and Brad Turner for their previous work in this research area. Finally, I'd like to thank the friends I've met along the way, who made all the hours in Kingsbury a bit easier.

TABLE OF CONTENTS

DEDICATION	III
ACKNOWLEDGEMENTS	IV
TABLE OF CONTENTS	V
TABLE OF TABLES	VII
TABLE OF FIGURES	VIII
ABSTRACT	XII
CHAPTER I: Introduction	1
1.1 Thesis Overview	4
CHAPTER II: Tube To Shaft Welding	7
2.1 Introduction & Motivation	7
2.2 Experimental Setup	8
2.3 Results	9
2.4 Discussion	12
CHAPTER III: Uniform Pressure Actuator: Analytical Design	14
3.1 Introduction & Motivation	14
3.2 Actuator Design Process	17
3.3 Model Results for Coil Design	34
3.4 Model Assumption Validation	42
3.5 Summary	48
CHAPTER IV: Uniform Pressure Actuator: Experimental Validation	50
4.1 Introduction	50
4.2 Actuator Construction	50

4.3 Experimental Setup.....	54
4.4 Photon Doppler Velocimetry	55
4.5 Results.....	58
4.6 Summary	70
CHAPTER V: Fiber Optic Displacement Sensor	72
5.1 Introduction.....	72
5.2 Sensor Characterization	73
5.3 Sensor Implementation.....	79
5.4 Discussion	86
5.5 Summary	89
CHAPTER VI: Conclusions and Future Work.....	91
6.1 Conclusions	91
6.2 Future Work.....	93
REFERENCES.....	94
APPENDIX A: ADDITIONAL EQUATIONS	97
APPENDIX B: MATLAB CODE	98

TABLE OF TABLES

<u>TABLE</u>	<u>PAGE</u>
Table 2.1: Tube to shaft MPW results.	12
Table 3.1: EMF machine and coil parameters.	35
Table 3.2: Key magnetic and mechanical response parameters.	36
Table 3.3: Johnson-Cook parameters for Al-6061-T6 [24].	43
Table 3.4: Mechanical FE analysis parameters.	44
Table 3.5: Mechanical FE analysis parameters.	47
Table 4.1: Heat treatment specifications for UNS C18000 after brazing of leads [26].	53
Table 4.2: Various workpiece thickness and α ratios with a skin depth of $\delta = 1.2mm$	66
Table 4.3: Material properties for workpiece conductivity experiments.	69

TABLE OF FIGURES

<u>FIGURE</u>	<u>PAGE</u>
Figure 1.1: Sample assemblies joined by MPW from PST Products a.) crimping of stranded copper wire, b.) dissimilar material drive shafts, and c.) Copper sheet welded between two Aluminum sheets [3].....	2
Figure 1.2: Diagram of the EMF & MPW [4].	3
Figure 2.1: Impact process during MPW [5].	7
Figure 2.2: Experimental setup for a tube to shaft MPW, showing a.) the shaft concentric with the tube, and b.) the six turn coil, Magneform leads, and insulating Kapton tape.	9
Figure 2.3: Welded assembly, showing cuts to examine whether welding occurred.....	9
Figure 2.4: Micrographs of the tube/shaft welded interface, at magnifications of a.) 50x, b.) 100x, and c.) 200x.	11
Figure 2.5: Wavelength and amplitude map for Explosive Welding (EXW), MPW, and Laser Impact Welding (LIW). Wavelengths and amplitudes are normalized by flyer workpiece thickness, t . Adapted from [2].....	13
Figure 3.1: Cross-section of the Uniform Pressure Actuator [9].....	15
Figure 3.2 Ohio State University UPA coil, second generation (left) and third generation (right) [12].....	17
Figure 3.3: Schematic of analytical solving process	19
Figure 3.4: EMF circuit diagram [13].....	21
Figure 3.5: Normalized current density for Cu 110 and SS321.....	22

Figure 3.6: 2D magnetic field geometry imposed on actual geometry (left), and 2D magnetic field representation, showing a single conductor and workpiece (right).	28
Figure 3.7: Predicted current and voltage, showing the half cycle time.	35
Figure 3.8: Predicted magnetic pressure and workpiece velocity.	36
Figure 3.9: Effect of k value [9] on the predicted magnetic pressure compared to the upper and lower bound solutions [20].	37
Figure 3.10: Aerodynamic effects on the workpiece acceleration, showing the drag ratio and mass ratio are more than two orders of magnitude smaller than the dominating effects.	38
Figure 3.11: Peak pressure and velocity generated for a given turn count.	40
Figure 3.12: Predicted pressure distribution across workpiece width varying with time.	41
Figure 3.13: FE analysis mesh and symmetry of workpiece, with 10mm die case shown.	43
Figure 3.14: Dynamic FEA comparison for center workpiece velocity with two die radii values.	45
Figure 3.15: Deformed workpiece with velocity resultant vectors from dynamic FE analysis. 10mm die case shown, at time $t = 64\mu s$	46
Figure 3.16: Von Mises stress from SolidWorks static mechanical FE simulation, showing fixed boundary conditions in green, and applied pressure in orange.	48
Figure 4.1: Pictures of a.) coil, and b.) the complete UPA assembly with PDV probe.	51
Figure 4.2: Dimensioned drawing of coil geometry (dimensions in mm).	52
Figure 4.3: Dimensioned drawing of return path geometry (dimensions in mm).	53

Figure 4.4: Coil potted in return path.	54
Figure 4.5: Experimental setup showing a.) the exterior and b.) the interior (i.e., in the forming box) details.	55
Figure 4.6: Schematic of a PDV system with target [27].	56
Figure 4.7: Experimental fit to current waveform during a 3.6kJ discharge and 1mm Al-6061-T6.	59
Figure 4.8: Comparison of initially predicted and experimental electrical parameters.	60
Figure 4.9: Electrical parameters' error on analytical model output of peak current and maximum velocity.	61
Figure 4.10: Modified experimental setup for measuring induced current in workpiece.	62
Figure 4.11: Primary and induced currents in the coil and workpiece.	62
Figure 4.12: Predicted velocities for varying k , with a 6kJ discharge and 1mm 6061-T6 workpiece.	63
Figure 4.13: Experimental velocity results from a 3.6kJ, 6kJ, and 8.4kJ discharge and 1mm Al 6061-T6 sheets, with the analytical model predictions shown for comparison.	64
Figure 4.14: Deformed 1mm 6061-T6 workpieces from a 3.6kJ, 6kJ, and 8.4kJ discharge energies, showing a.) front view (i.e., view normal to coil axis) and b.) side view (i.e., coil turns across photograph).	65
Figure 4.15: Workpiece velocity with varying workpiece thicknesses and analytical model prediction. Discharge energy was 6kJ.	67
Figure 4.16: Workpiece velocity with varying workpiece conductivity and analytical model prediction. Discharge energy was 6kJ.	69
Figure 5.1: Reflectance dependant, fiber optic sensor operation schematic [30].	73

Figure 5.2: Experimental setup for sensor characterization.....	74
Figure 5.3: Calibration curve for flat, mill-finish aluminum surface.....	74
Figure 5.4: Experimental setups for angular effects: a.) flat surface, b.) horizontal Cylinder, and c.) vertical cylinder.....	75
Figure 5.5: Gap distance error induced from angular effects for three experiments: flat surface, horizontal cylinder, and vertical cylinder.	76
Figure 5.6: Calibration to flat surface with retroreflective tape applied and a with mill-finish Aluminum surface.....	78
Figure 5.7: Angular effects on flat surface with retroreflective tape applied and a mill-finish Aluminum surface.	79
Figure 5.8: Experimental setup for UPA flat sheet forming tests.	80
Figure 5.9: Velocity results for 1mm sheet Al 6061-T6 forming at 3.6kJ, 6kJ, and 8.4kJ discharge energies, measured with the fiber optic sensor and the PDV system.	81
Figure 5.10: a.) Front view and b.) side view of deformed workpiece with a 6.0kJ discharge, with the location of the fiber optic sensor indicated.	82
Figure 5.11: a.) Experimental setup for tube/shaft welding in forming box and b.) Cross section view of single turn coil (dimensions are in mm).....	84
Figure 5.12: Velocity results for 25.4 mm diameter, .89 mm wall, 2024-T3 tubes at various energy levels, measured with a.) the fiber optic sensor and b.) the PDV system.	85
Figure 5.13: Deformed workpiece with a 9.6kJ discharge, with the location of the fiber optic sensor indicated.	86
Figure 5.14: Translation calibration with deformed specimen and damaged retroreflective tape.	88

ABSTRACT

DEVELOPMENT OF ANALYTICAL AND EXPERIMENTAL TOOLS FOR MAGNETIC PULSE WELDING

By

Ethan Hunter Thibaudeau

University of New Hampshire, September 2013

Degree Advisor: Brad Kinsey

A key process parameter in magnetic pulse welding (MPW) is the workpiece velocity, and while some Finite Element Analysis (FEA) packages exist that are capable of modeling these processes, there is a lack of simplified analytical modeling efforts, which are attractive for their simplicity and cost. In this work, an electromagnetic actuator, named a Uniform Pressure Actuator (UPA), is analyzed, designed, constructed, and tested experimentally. The analytical model is shown to predict workpiece velocities accurately and produce an efficient forming and a robust design. Additionally, an alternative method to measure workpiece velocity is presented, implementing a fiber optic, reflectance dependent sensor. The sensor is shown to be an attractive low cost solution to measurement of high velocities in high voltage, magnetic environments, through experimental measurement in parallel with a Photon Doppler Velocimetry (PDV) system.

CHAPTER I

INTRODUCTION

Electromagnetic forming (EMF) is a high-speed metal forming process that uses pulsed magnetic fields to create non-contact plastic deformation of metallic workpieces during the acceleration process. Typical workpiece velocities on the order of 100-300 m/s are produced, and when impacted into a die, large impact pressures further deform the workpiece. Benefits of EMF include improved formability, uniform strain distributions, reduction in wrinkling, active control of springback, and the possibility of local coining and embossing [1].

The need for both strong and lightweight components and assemblies exists in several industries (e.g., automotive, aerospace, electronics, etc.). For individual components, this can be achieved through composites, lightweight alloys, Advanced High Strength Steels, etc. But for assemblies, the joining of components with vastly different material properties (e.g., melting temperature) by fusion welding is not feasible. An alternative means to create a welded joint is through solid state Magnetic Pulsed Welding (MPW).

If a second, stationary workpiece is impacted at a critical impact velocity and angle, a solid state weld is produced at the interface through this MPW process. Joining can be achieved even between base metals of vastly different material properties, and bond strength is typically stronger than the parent components [2]. This allows joined components in an assembly to be tailored to a specific

function according to material properties, and assembly weight is reduced from removing fasteners. The final assembly's overall dimensional accuracy is controlled by fixturing of the individual components. However, in the weld region, joint strength is typically more of a concern than final geometry (e.g., the final diameter of a crimped section of a tube that has been welded to a shaft).

MPW is well suited for large series production of assemblies that require a weld for strength and/or a permanent seal. Examples of this include enclosures for automotive filters and pressure capsules. MPW can be implemented to join torque transmitting assemblies, where the end components may be a different material than the middle component. MPW can also be implemented to join sheet metal components for electrodes in batteries and capacitors [3]. Figure 1.1 shows examples of assemblies created with this process. Other processes that use the same joining mechanism, include Laser Impact Welding (LIW) for smaller length scale components, and Explosive Welding (EXW) for larger scale components [2].

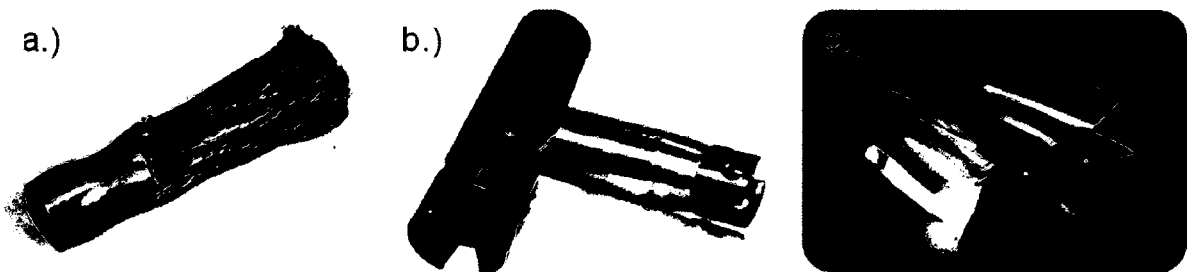


Figure 1.1: Sample assemblies joined by MPW from PST Products a.) crimping of stranded copper wire, b.) dissimilar material drive shafts, and c.) Copper sheet welded between two Aluminum sheets [3].

In EMF and MPW, a pulsed power supply discharges into coil which creates a magnetic field in close proximity to the workpiece. Eddy currents are induced in

the workpiece, and a repulsive Lorentz force is created from the magnetic field - eddy current interaction which causes the workpiece to accelerate away from the coil and plastically deform. Typical measurements of the processes include primary and induced currents in the coil and workpiece, respectively, and workpiece displacement and velocity. Figure 1.2 shows a schematic of the EMF/MPW process [4].

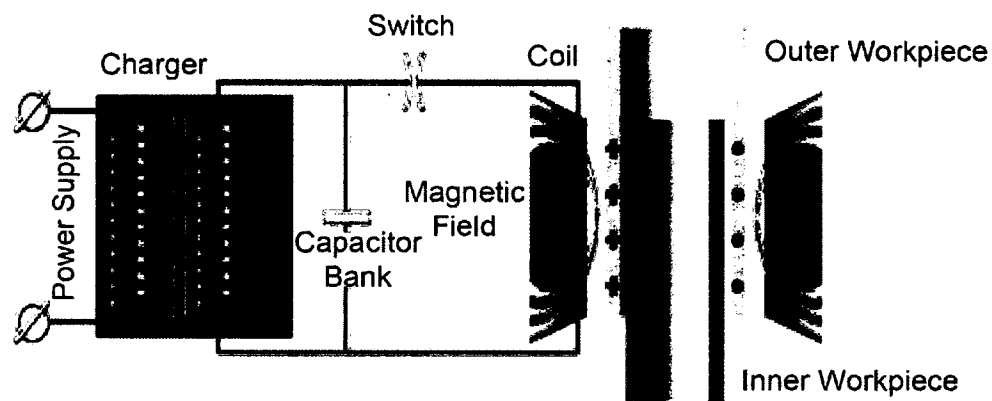


Figure 1.2: Diagram of the EMF & MPW [4].

The reported efficiency of EMF & MPW processes varies widely, depending the forming and welding geometry, and the coil design. Energy that is initially stored in the capacitors is eventually transformed into deformation energy of the workpiece by the end of the process, however losses occur from intermediate energy transfers. From the initially stored energy, Joule heating reduced the amount of available electrical energy, e.g., heating in the lines connecting the capacitor bank to the coil, in the coil, and in the workpiece. Magnetic losses occur from leakage of magnetic flux further decrease the energy available to accelerate the workpiece, e.g., due to imperfect coupling between the coil and workpiece.

1.1 THESIS OVERVIEW

In Chapter II, a tube to shaft welding process is presented to observe the wavy interface that forms in a MPW. Disposable coils are implemented as a cost effective, proof-of-concept for MPW. Large currents, and thus large magnetic pressure is developed in these coil, which creates the impact pressure necessary for welding, but also destroys the coil in the process. Micrographs are taken of the welded region to observe the wavelength and amplitude of the weld, as well as the impact angle necessary for welding.

In Chapter III, a coil design and analysis procedure developed at The Ohio State University is modified and extended through an analytical model, with some stages of analysis verified with FEA. The coil, named a Uniform Pressure Actuator (UPA), offers increased forming efficiency and repeatability, as well as a robust design. Coil design parameters such as the number of turns and conductor cross section are determined for a given workpiece. Magnetic pressure applied to the workpiece and workpiece velocity are predicted to ensure impact velocities are sufficient for MPW.

In Chapter IV, the UPA was constructed and tested experimentally to validate the accuracy of the analytical model, as well as verify the remaining assumptions made during modeling. Experiments to compare the predicted electrical parameters of the UPA were conducted, and show sufficient accuracy for the purpose of predicting workpiece velocity. The coupling coefficient introduced in the magnetic analysis is experimentally determined and compared to previous

researcher's values. Workpiece velocities for various energy levels, workpiece thicknesses, and materials with various conductivities and densities are compared to analytical predictions and show good agreement for the initial acceleration process which lasts approximately to peak velocity. Workpiece velocity measurements are performed with Photon Doppler Velocimetry (PDV), which provides a robust method for measuring velocities with submicron displacement resolution and temporal resolution in the nanosecond range. Uniformity of the workpiece deformation is also examined, which is an advantage of the UPA.

In Chapter V, an alternative method for high velocity measurements is presented, implementing a fiber optic, reflectance dependent displacement sensor. The sensor is shown to be an attractive low cost solution to measurement of high velocities in high voltage, magnetic environments. Data is shown with respect to sensor characterization including various surface reflectivity values, curvatures, and misalignments; implementation in two forming/welding processes; and verification with high velocity measurement in parallel with PDV. The sensor system is one twentieth the cost of a PDV system, and yet measures velocities accurately to at least 150 m/s provided that local deformations do not cause excessive curvatures. Sensor performance is also enhanced by the use of retroreflective tape, which is shown to increase the displacement range by 9x, decrease sensitivity to misalignment, and increase repeatability and ease of implementation.

The major outputs/findings from this research are:

- An analytical model for designing a UPA for sheet metal forming/welding (e.g., the number of coil turns) and predicting workpiece velocity,
- Measurement of a magnetic coupling coefficient for the UPA, which is independent of material thickness and conductivity, provided the workpiece thickness to skin depth ratio is near unity,
- Implementation of a UPA with validated velocities compared to analytical model results,
- Alternative method for high velocity measurement using a fiber optic displacement sensor which is a fraction of the cost, safer, and easier to implement.

CHAPTER II

TUBE TO SHAFT WELDING

2.1 INTRODUCTION & MOTIVATION

In order to investigate MPW, an initial process was implemented where a Aluminum tube was crimped and welded to a Aluminum shaft. The axisymmetric geometry allows for a simpler work coil design, where coils were hand wound from thin copper wire. This provided an inexpensive, proof-of-concept experimental setup to produce a MPW for the given geometry.

The coil does not survive the process due to the high mechanical and electrical loads applied. Disposable coils are advantageous since larger instantaneous powers can be achieved. This produces the large workpiece acceleration and impact velocity required for MPW. Another key parameter in MPW is the impact angle between the flyer and stationary workpiece, as shown in Figure 2.1).

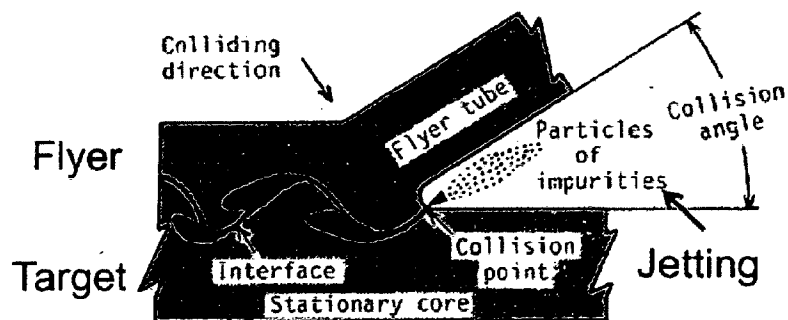


Figure 2.1: Impact process during MPW [5].

The drawback to this method is that the setup time for each test is increased from hand winding and insulating work coils. Additionally, the long term cost is greater for disposable coils than it is for robust coils that last many welding operations.

2.2 EXPERIMENTAL SETUP

A 25.4mm diameter, 1mm thick Al 6061-T6 tube was placed over a 20.9mm diameter Al 2024 shaft. 10 AWG magnet wire was hand wound around a mandrel to produce a tight fit when positioned around the 25.4mm tube. The magnet wire used was Cu101 solid wire, with a insulative enamel coating pre-applied. A 6 turn coil resulted in an axial coil length of 15.5mm. The outer surface of the shaft and inner surface of the tube were sanded with 200 grit sandpaper, and cleaned with isopropyl alcohol. See Figure 2.2 for an image of the experimental setup.

Kapton tape was used to insulate the workpiece from the high voltages produced in the work coil, and to position the shaft concentric with the tube. A 10.8kJ discharge was applied to the coil, which created magnetic forces that accelerate and impact the tube into the shaft. A 12kJ capacity Maxwell Magneform 7000 JA was used to generate the electrical discharge.

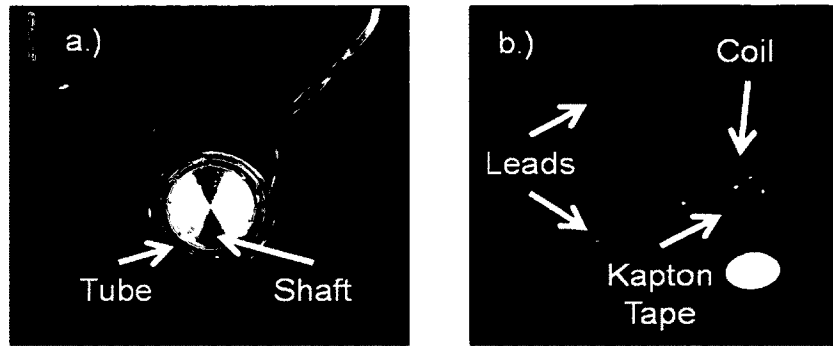


Figure 2.2: Experimental setup for a tube to shaft MPW, showing a.) the shaft concentric with the tube, and b.) the six turn coil, Magneform leads, and insulating Kapton tape.

2.3 RESULTS

Results show that welding occurs at a critical impact angle during the deformation. This forming geometry produced two axial welding locations where the correct impact angle was created. The assembly was examined for welds by making two cuts, as shown in Figure 2.3.

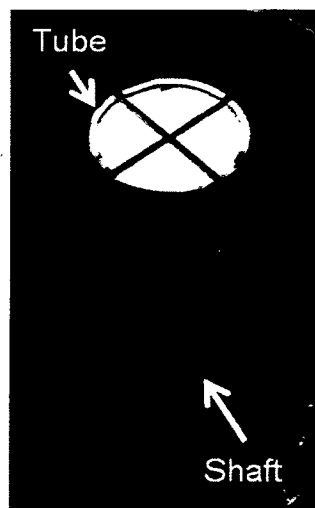


Figure 2.3: Welded assembly, showing cuts to examine whether welding occurred. A third cut was made to create quarter sections, that were polished, etched, and micrographed to examine the tube/shaft interface. At all locations where the tube was welded to the shaft, a wavy interface was produced. Figure 2.4a shows a

micrograph of one quarter section, with two axial welding locations. The largest amplitude observed in the weld was $33\mu m$, and the largest wavelength was $212\mu m$.

As an artifact of the etching process, the axial center of the interface shows black regions where the etchant remained trapped and removed additional material (these regions were not observed before etching). In this view, the impact angle that was formed during impact is shown, and welding occurred at this angled interface. Figure 2.4b and Figure 2.4c show additional magnification levels of one of the welding locations.

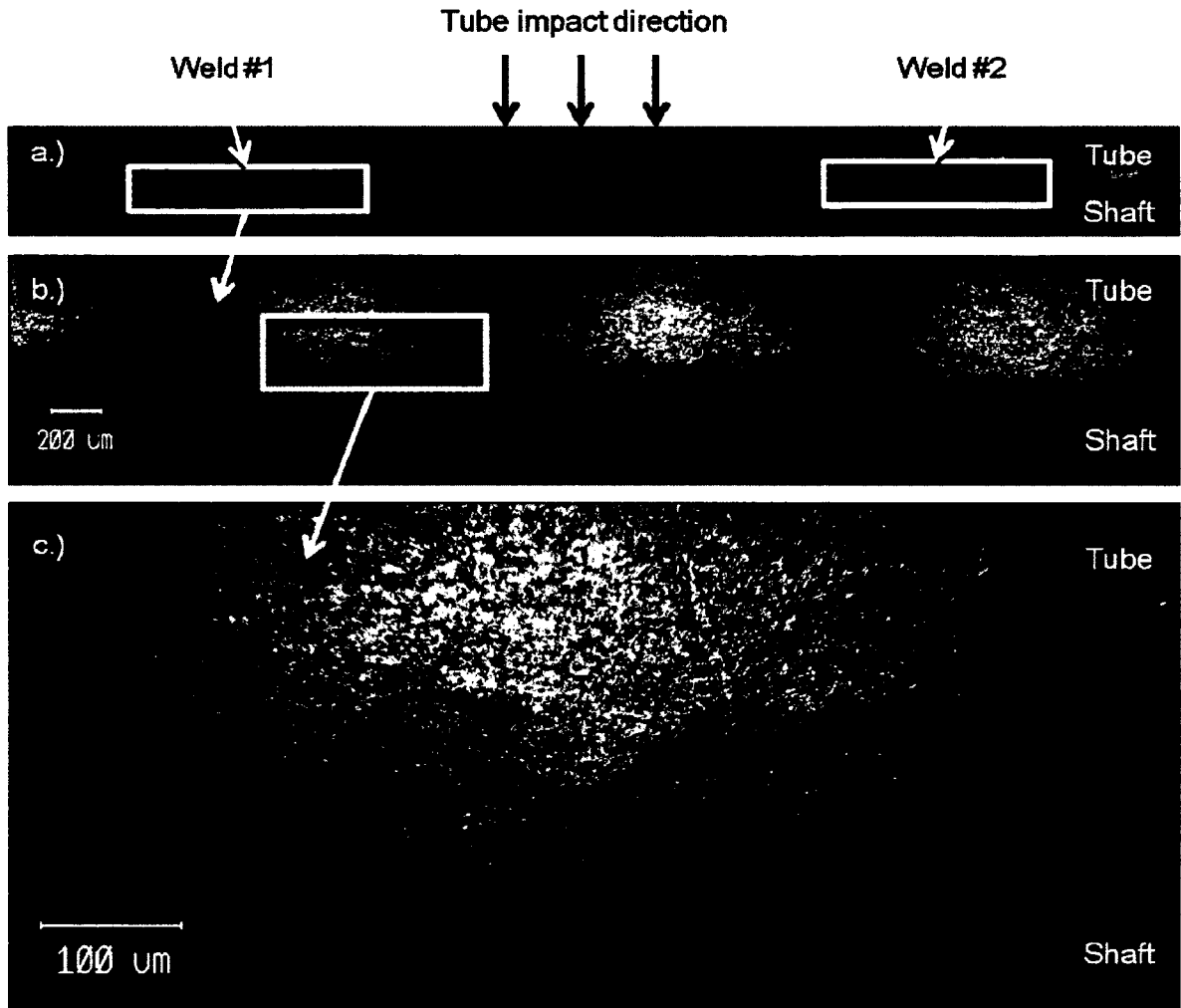


Figure 2.4: Micrographs of the tube/shaft welded interface, at magnifications of a.) 50x, b.) 100x, and c.) 200x.

The impact angle was formed during the tube impact due to the non-uniform magnetic pressure distribution in the coil. Larger pressure was generated in the center turns of the coil, so the axial center of the tube was accelerated at a higher rate, which impacted and plastically deformed the shaft. As the plastic deformation of the shaft proceeded, it created the impact angle necessary for welding the outer axial regions. The angle of the weld relative to the shaft axis was measured from the micrographs in Adobe Photoshop. Table 2.1 lists the weld locations and their corresponding angle.

Table 2.1: Tube to shaft MPW results.

Circumferential Location	Axial Location			
	Weld #1		Weld #2	
	Weld	Angle (°)	Weld	Angle (°)
1	Yes	2.3	No	-
2	Yes	1.9	Yes	3.2
3	Yes	4.8	Yes	3.3
4	Yes	2.7	No	-

2.4 DISCUSSION

As an initial investigation, a simple and inexpensive experimental setup produced a MPW on a tube/shaft interface. This setup shows that the required impact angle can be created during the process by the magnetic pressure distribution and the deformation. Therefore, geometrical modification of workpieces is not necessary to achieve a MPW, but continuous welding along the axis (as shown in Figure 2.4) will not be achieved.

When normalized by the tube thickness, the observed wavelength and amplitude agree with previous research [2]. Figure 2.5 shows these normalized parameters for various impact welding processes, adapted from [2] to include our experimental results.

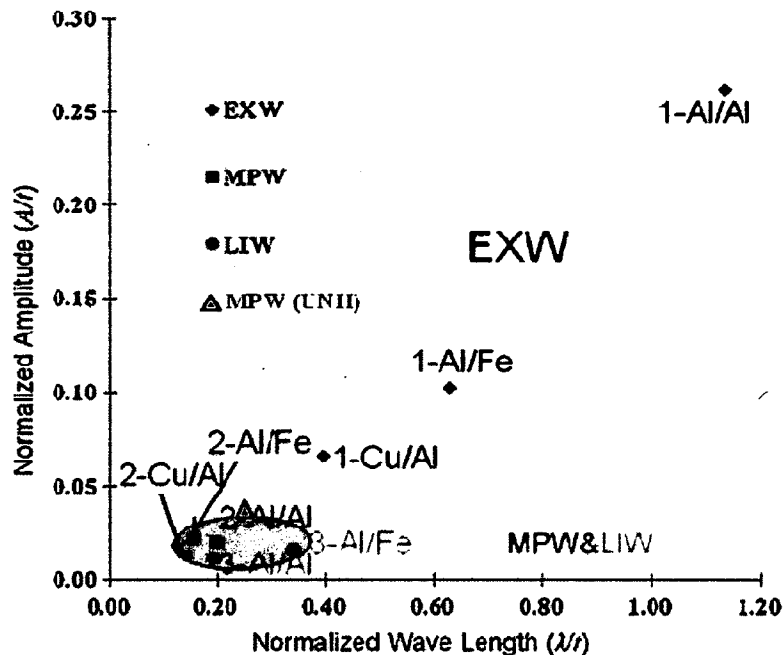


Figure 2.5: Wavelength and amplitude map for Explosive Welding (EXW), MPW, and Laser Impact Welding (LIW). Wavelengths and amplitudes are normalized by flyer workpiece thickness, t . Adapted from [2].

However, there are some disadvantages to this experimental setup. Due to the geometry of coil, and its disposable nature, measurements of impact velocity could not be performed. Additionally, only the final interface angle can be observed, which may vary from the actual impact angle during the process due to plastic deformation. Axisymmetric welding/crimping joints are also difficult to access, since a destructive test is required to observe the presence of a weld.

These disadvantages present additional motivation for research in sheet metal welding. In the two following chapters, a new coil is designed and constructed to form and weld sheet metal. The robust design allows for a high level of repeatability, and if a weld is produced, its location between two sheets allows easy assessment of the strength of the weld.

CHAPTER III

UNIFORM PRESSURE ACTUATOR: ANALYTICAL DESIGN

3.1 INTRODUCTION & MOTIVATION

Axisymmetric crimping and welding of tubes and shafts have experienced the most implementation of EM processes. However, for lightweight automotive applications, forming and welding of flat sheets is of interest. Development of work coils and process analysis for sheet forming has been limited due to its complexity [1]. According to Daehn, a gap exists between experts in sheet metal forming and in pulsed power applications [6]. Therefore, simplified modeling acts to bridge this gap and promote EM applications in manufacturing.

In past research, forming and welding of flat sheet workpieces was achieved with a few different coil designs. Flat spiral coils have been implemented, where a wire is wound in a flat spiral, in a plane parallel to the workpiece. However, they typically fail after a small number of forming operations [7]. Additionally, the pressure distribution across the workpiece is non-uniform with the peak pressure at half of the coil planar radius which leads to ripples in the workpiece deformation [1].

Single or half turn coils have also been used for welding sheets, but the pressure distribution is localized in a small region [8]. Kamal et al. [9] developed a coil design, i.e., a Uniform Pressure Actuator (UPA), which has a more uniform

pressure distribution over a larger area and is robust enough to last hundreds of forming operations. The design consists of a helical coil with a rectangular cross-section. A surrounding conductive channel allows induced eddy currents in the sheet to form a closed circuit around the coil. A cross-section schematic of this assembly is shown in Figure 3.1.

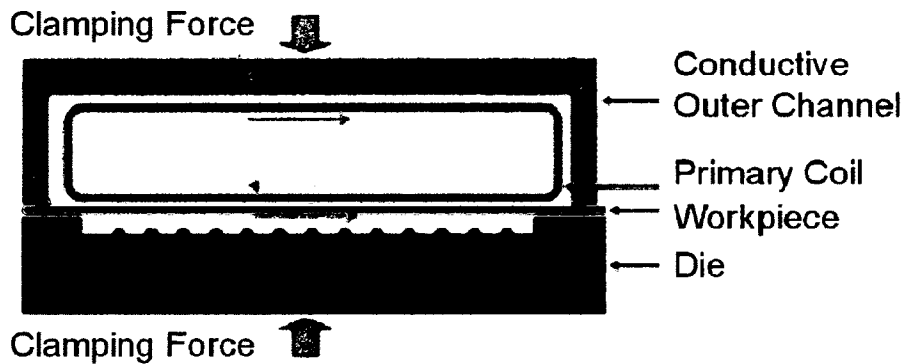


Figure 3.1: Cross-section of the Uniform Pressure Actuator [9].

The return path integrated into the coil design has multiple advantages. Since eddy currents generated in the workpiece flow in a closed circuit, edge effects of the sheet are eliminated as eddy currents flow throughout the workpiece. Also, additional eddy currents are generated from the coil and return path, which create a higher magnetic pressure. By including the return path, the magnetic field generated around the entire coil is put to use in the forming process increasing the efficiency of the process [9]. Finally, repulsive forces generated between the helical coil and return path help to resist the radial forces generated by the coil on itself, thus increasing the strength of the actuator.

In order to model the transient EMF/MPW process, and thus design the coil, analytical and FE analysis have been used. For example, Zhang et al. [2] used

the commercial finite element (FE) code, LS-DYNA to solve the electromagnetic, mechanical, and thermal problem, in a fully coupled manner for the magnetic fields, induced eddy currents, workpiece acceleration, and high velocity impact of the workpiece. Other commercially available packages are capable of solving the electromagnetic and mechanical problem, such as ANSYS [10] and ABAQUS [11].

Kamal et al. [12] presents an EMF model focusing on coil design and is comprised of an analytical model and FE magnetic modeling in 2D. The deformation of the workpiece was solved separately in LS-DYNA. The analytical model predicted rigid body workpiece acceleration, and is attractive for its simplicity and cost in effectively determining a optimal coil design.

As shown by Kamal [12] a large coil turn count results in a stronger magnetic field, and thus higher magnetic pressure. However, a small turn count allows for a shorter rise time to peak current. Therefore, it is important to specify whether the coil design is aimed at creating maximum pressure or maximum sheet velocity. Forming shallow features or embossing requires larger pressures, whereas deep features and larger deformations require higher velocities to create large inertial effects and high impact pressures [9].

In this chapter, the design analysis for a UPA was modified and extended [9] through an analytical model in order to maximize the magnetic pressure and workpiece velocity. The pressure distribution over the workpiece and a rigid body motion assumption were investigated. Also, finite element (FE) analysis was

used to access the robustness of the coil design. Finally, the coil was constructed and implemented in a free forming process.

3.2 ACTUATOR DESIGN PROCESS

Prof. Glenn Daehn's group from The Ohio State University developed multiple generations of UP actuators, shown in Figure 3.2. Initially, their construction consisted of soft copper windings around an insulating mandrel. Further generations moved to a stronger design, with a thicker coil cross section, machined out of a solid block of high strength copper alloy. The coils were then potted in urethane for electrical insulation.



Figure 3.2 Ohio State University UPA coil, second generation (left) and third generation (right) [12].

Kamal et al. [12] presented an EMF model focusing on coil design and is comprised of an analytical model and FE magnetic modeling in Maxwell 2D. The deformation of the workpiece was solved separately in LS-DYNA. The analytical model predicted rigid body workpiece acceleration, and is attractive for its simplicity and cost in effectively determining an optimal coil design.

A large coil turn count results in a stronger magnetic field, and thus higher magnetic pressure. However, a small turn count allows for a shorter rise time to peak current [12]. Therefore, it is important to specify whether the coil design is to create maximum pressure or maximum sheet velocity. Forming shallow features or embossing requires larger magnetic pressures, whereas deep features with large deformations requires higher velocities to create large inertial effects and high impact pressures [9].

The research by Kamal et al. [12] is the basis of the model presented here. The goal is to determine, for a given sheet geometry, a coil geometry that maximizes pressure or sheet velocity, while maintaining structural integrity.

Compared to Kamal et al., an alternative design process is conducted that consists of an analytical model and a FEA structural analysis. The analytical model calculates the initial workpiece acceleration of the EMF/MPW process. Magnetic pressure and rigid body workpiece acceleration are solved for a given UPA geometry, workpiece length, and coil turn count. A FE mechanical analysis determines if the resultant geometry is strong enough to withstand the predicted magnetic pressure. If the mechanical simulation shows material failure, the analytical model is used to modify the geometry. For a given workpiece length, a larger conductor cross-section, and thus lower turn count, produces a more robust coil.

3.2.1 ANALYTICAL MODEL

The analytical model used in this research can be divided into stages based on the type of physical interaction involved. First, electrical theory is used to determine the current out of the EMF machine and through the coil. Second, electromagnetic analysis determines the magnetic field distribution and the effective magnetic pressure that is developed on the workpiece. Lastly, classical mechanics theory is used to find rigid body motion of the workpiece caused by the magnetic pressure. The magnetic and mechanical processes are loosely coupled in this model (i.e., at each increment in time, the magnetic field geometry is updated from the workpiece displacement). See Figure 3.3 for a schematic of this solving process.

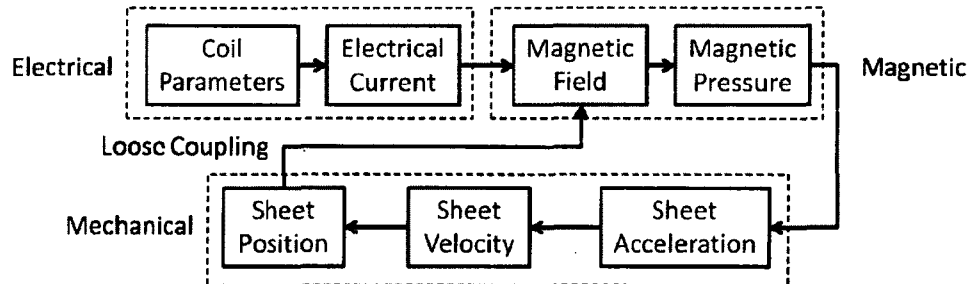


Figure 3.3: Schematic of analytical solving process

In terms of geometry, the coil turn count and required spacing for electrical insulation act as inputs to the model, and the conductor width is the output. The effect of the number of turns in the coil was determined by running the analytical model with varying numbers of coil turns. Maximum magnetic pressure and maximum sheet velocity are both affected by the number of turns [12], which can be observed in the results. Pressure variation on the workpiece can also be

observed from this model, (i.e., the necessary spacing of turns for an even pressure distribution).

3.2.2 ELECTRICAL THEORY

The primary electrical circuit, consisting of a capacitor bank, coil, and workpiece, can be represented by ideal electrical elements (i.e., resistors, capacitors, and inductors). Past researchers have presented electrical models of varying degrees of complexity. Bauer [13] presented a series RLC (Resistance-Inductance-Capacitance) circuit that included a mutual inductance, M , between the coil and workpiece, as shown in Figure 3.4. The mutual inductance, in the case of imperfect magnetic coupling, can be found from [14]:

$$M = k\sqrt{L_c L_w} \quad (3.1)$$

where L_c and L_w are the inductance of the coil and the workpiece, respectively, and k is the geometric dependant coupling coefficient. The coupling coefficient represents the leakage of magnetic flux from the alignment of the two inductors, with a value between $0 \leq k \leq 1$. Jablonski [15] reduced the mutually coupled model by assuming that the workpiece inductance was negligible (i.e., $L_w \approx 0$). This simplification is valid when the inductance of the workpiece is small, which is the case for typical tubular and sheet workpieces.

The EMF machine is largely represented by a capacitance, but internal resistance and inductance are also included. Conversely, the coil is primarily an inductance element, but an internal resistance is also included. Resistance and inductance values of the EMF machine, (R_m and L_m) can be determined

experimentally by recording the electrical response to a shorted load. Resistance and inductance values for the coil (R_c and L_c) are calculated from the geometry for the purposes of UPA design, but they can also be determined in the same manner as the EMF machine once the coil exists (i.e., $R_c = R - R_m$), since the resistive elements are in series.

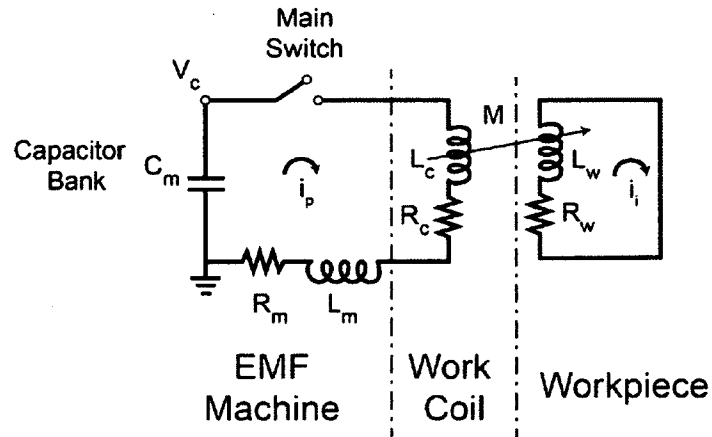


Figure 3.4: EMF circuit diagram [13].

The inductance of the coil can be calculated as that of a rectangular current sheet, with corrections for non-conducting space and finite conductor cross section [16]. A working formula for a rectangular coil can be found in Appendix A, Equations 7.1 and 7.2. The inductance is determined from that of the coil geometry only; therefore, effects of the return path and workpiece are neglected [15].

Since the current is oscillating, the skin effect produces an exponentially decaying current density distribution, J , from the surface current density, J_s , in the conductor cross section. The distribution is governed by [17]:

$$J = J_s e^{-d/\delta} \quad (3.2)$$

where d is the depth into the conductor, and the skin depth, δ , is defined as [17]:

$$\delta = \sqrt{\frac{2\rho}{\mu_0\mu_r\omega}} \quad (3.3)$$

where ω is the frequency of the current through a conductor of resistivity ρ , μ_r is the relative magnetic permeability of the conductor, and μ_0 is the magnetic permeability of free space. To illustrate the skin effect, the current density is shown on the geometry of a Cu 110 and SS 321 cylindrical conductor in Figure 3.5, with $\omega = 8.1 \times 10^4 \text{ rad/s}$, $\mu_r = 1$, and a 5mm radius. Although typical MPW geometries are rectangular, a cylindrical geometry is the simplest to illustrate the skin effect. Additionally, the current density in this example is normalized with a surface current density of $J_s = 1$.

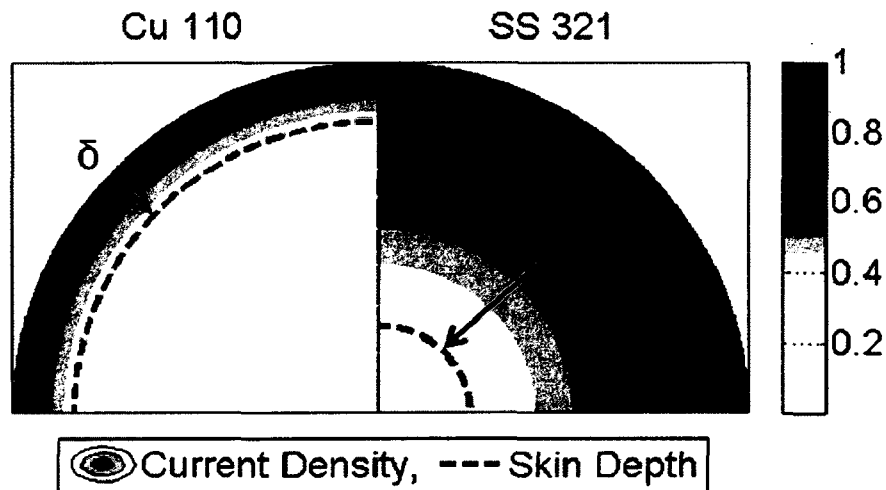


Figure 3.5: Normalized current density for Cu 110 and SS321.

The exponential distribution of current density causes a reduction in the effective conductor cross section. The resistance of a conductor subjected to alternating current, R_{AC} , can be determined by substituting an effective cross sectional area, A_{eff} , into the resistance of a conductor when subjected to direct current [17]:

$$R_{DC} = \rho \frac{L}{A_{eff}} \quad (3.4)$$

where L is the conductor length and A_{eff} is the cross-sectional area contained from the skin depth (δ) to the surface of the conductor (i.e., all of the current flows within one skin depth). This approximation is valid as long as the skin depth is small compared to the conductor thickness [17]. Otherwise, corrections are available for when the skin depth is of comparable length to the thickness of the conductor [18].

The transient response of the primary circuit is determined by measuring EMF machine circuit parameters, calculating coil parameters, applying initial conditions, and solving the governing differential equation. Applying Kirchhoff's voltage law [19] and summing the voltages around the circuit, a differential equation is obtained with respect to time, t :

$$\frac{1}{C} \int i_p dt + iR + L \frac{di_p}{dt} = 0 \quad (3.5)$$

where R , L , and C are the respective total resistance, inductance, and capacitance in the circuit and i_p is the current in the primary circuit.

Initial conditions of the differential equation are found from the charged capacitor with main switch closing at $t = 0$. When the current is initially zero, there is no voltage drop across the resistor. Therefore the voltage across the inductor will become that of the capacitor, so the initial conditions are:

$$i_p(0) = 0, \quad \frac{di_p}{dt}(0) = \frac{V_{co}}{L}, \quad (3.6)$$

where V_{co} is the initial voltage on the capacitor.

By solving the differential equation, Equation (3.5), with the initial conditions in Equation (3.6), the primary circuit current, $i_p(t)$, is obtained as [19]:

$$i_p(t) = \frac{V_{co}}{\sqrt{1-\zeta^2}} \sqrt{C/L} e^{-\zeta\omega_n t} \sin \omega_n \sqrt{1-\zeta^2} t \quad (3.7)$$

where ω_n is the natural frequency of the circuit:

$$\omega_n = \frac{1}{\sqrt{LC}} \quad (3.8)$$

and ζ is the damping ratio of the circuit:

$$\zeta = \frac{R}{2} \sqrt{\frac{C}{L}} \quad (3.9)$$

To check the accuracy of the predicted total parameters, R , L , and C , tests can be performed experimentally where ζ and the damped natural frequency, ω_d , can be determined by measuring the current waveform. That is, ζ is determined from the exponential decay of current amplitude through the log decrement method [19], and ω_d is simply the frequency of the current waveform. The following relation allows us to determine ω_n from ω_d and ζ :

$$\omega_n = \frac{\omega_d}{\sqrt{1-\zeta^2}} \quad (3.10)$$

With the capacitance of EMF machine known, Equation (3.8) can be rearranged to determine L :

$$L = \frac{1}{\omega_n^2 C} \quad (3.11)$$

and with L known, R can be determined by rearranging Equation (3.9):

$$R = 2\zeta \sqrt{\frac{L}{C}} \quad (3.12)$$

Lastly, capacitor voltage, V_c , can be calculated by integrating the current out of the capacitor:

$$V_c(t) = \int -i_p(t)dt + V_{co} \quad (3.13)$$

3.2.3 MAGNETIC THEORY

The magnetic field produced from a given coil geometry and electrical current can be determined with respect to the physical location along the coil, time, and the gap distance between the coil and workpiece. The calculation of the magnetic field strength is simplified by assuming a super conducting workpiece. Al Hassani [20] states that this is an appropriate approximation for highly conductive metals typically used in EMF, such as copper or aluminum. However, to account for finite workpiece resistance, an experimentally determined correction coefficient [9], k , which represents the magnetic coupling shown in Figure 3.4.

The magnetic flux density, \vec{B} , produced by the coil induces eddy currents in the workpiece to produce a current density, \vec{j} . A Lorentz force is created which acts as a volume force, \vec{F} , [1]:

$$\vec{F} = \vec{j} \times \vec{B} \quad (3.14)$$

It is this Lorentz force acting as a body force that creates workpiece acceleration and deformation. Since we are concerned with the force in the thickness

direction, y , the current density, \vec{J} , is related to the magnetic field, \vec{H} , through a partial derivative in that direction [1]:

$$\vec{J} = -\frac{\partial \vec{H}}{\partial y} \quad (3.15)$$

In non-magnetic materials, a constitutive relation exists between the magnetic field, \vec{H} , and the magnetic flux density, \vec{B} , such that:

$$\vec{B} = \mu \vec{H} \quad (3.16)$$

where μ is the permeability of the material. Therefore, the Lorentz force becomes [1]:

$$\vec{F} = -\mu \vec{H} \frac{\partial \vec{H}}{\partial y} = -\frac{1}{2} \mu \frac{\partial (\vec{H}^2)}{\partial y} \quad (3.17)$$

The body force, \vec{F} , is integrated through the thickness of the workpiece to determine an effective pressure acting on the workpiece surface, (i.e., a magnetic pressure), P_m , [1]:

$$P_m = \int_{y_1}^{y_2} \vec{F} dy = \frac{1}{2} \mu (H_{gap}^2 - H_{pen}^2) \quad (3.18)$$

where the integration limits, y_1 and y_2 are the workpiece thickness edges, and H_{gap} and H_{pen} are the gap region and penetrated magnetic field strengths, respectively. For simplification, the workpiece can be approximated by either a superconducting ($\rho = 0$) or highly resistive half space ($\rho = \infty$). With a superconducting workpiece, the penetrated field strength is neglected due to the skin effect [1], so that the magnetic pressure is:

$$P_m = \frac{1}{2} \mu H_{gap}^2 \quad (3.19)$$

To simplify the calculation of H_{gap} , the coupling coefficient, k , is introduced (see Equation (3.1)) to account for the level of magnetic coupling between the coil and workpiece. The magnetic pressure now becomes [9]:

$$P_m = \frac{1}{2} \mu k H_{gap}^2 \quad (3.20)$$

The coupling coefficient was determined experimentally by Kamal et al. [9] for various workpiece materials for their UPA (i.e., $k = 0.7$ for an Aluminum workpiece, and $k = 0.55$ for a stainless steel workpiece). Alternatively, Xu et al. [21] determined $k = 0.09$ for a flat spiral coil with no return path, and a Aluminum workpiece.

Experimentally, k can be determined by measuring the primary and induced currents in the coil and workpiece, respectively. The coupling coefficient can be found from [9]:

$$k = \frac{i_i}{n i_p} \quad (3.21)$$

where i_i is the induced current in the workpiece, and n is the number of turns in the coil.

Additionally, the air space and insulation material between the coil and workpiece is not considered in the magnetic calculation. Their respective relative permeability are close to that of free space, so their effect on the magnetic field is negligible. The effect on the magnetic field from the return path is also not included for simplicity.

The magnetic field strength, H_{gap} , is the resultant field of a superposition of magnetic field strength from many current carrying differential elements, dH_{gap} . Each element is assumed to be in proximity to that of an infinitely conducting half space ($\rho = 0$), which represents an upper bound for the magnetic field prediction. With this geometry, H_e is purely tangential to the workpiece surface, so only the x component is of interest (i.e., $H_{e,x}$). $H_{e,x}$ was determined by Al-Hassani [20]:

$$H_{e,x} = \frac{i}{2\pi} \left[\frac{g-y}{(g-y)^2 + x^2} + \frac{g+y}{(g+y)^2 + x^2} \right] \quad (3.22)$$

where, x and y are coordinate dimensions, and g is the gap between the conductor and sheet shown in Figure 3.6. The current in each element, i , is assumed to be spatially uniform through each of the differential elements. Diagrams of the coil and workpiece 3D geometry and 2D representative geometry are shown in Figure 3.6.

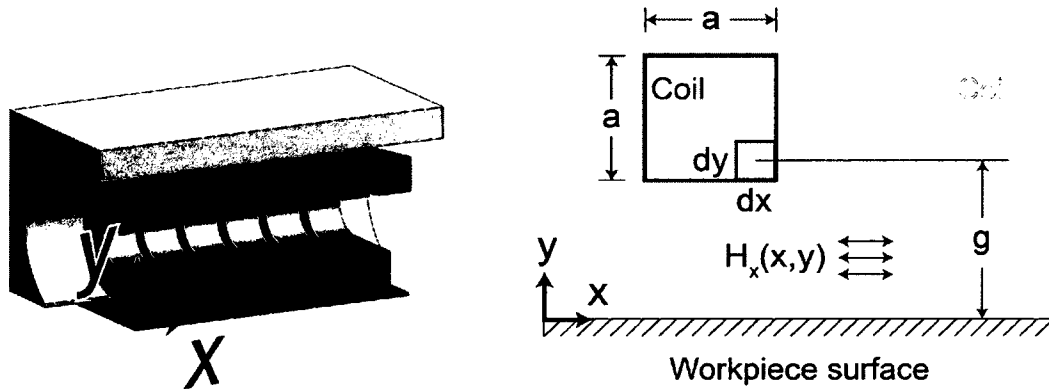


Figure 3.6: 2D magnetic field geometry imposed on actual geometry (left), and 2D magnetic field representation, showing a single conductor and workpiece (right).

Al-Hassani also showed the effect of exchanging the infinitely conducting half space ($\rho = 0$) to a infinitely resistive half space ($\rho = \infty$). $H_{e,x}$ was determined for this case [20]:

$$H_{e,x} = \frac{i}{2\pi} \left[\frac{g+y}{(g+y)^2 + x^2} \right] \quad (3.23)$$

This represents a lower bound for the magnetic field.

To determine the contribution to the magnetic field from a single conductor, differential elements are integrated to determine the x component of the magnetic field. For an element of height, dy , and width, dx , each element has the current:

$$i = i_p dx dy / a^2 \quad (3.24)$$

where a is width and height of a square conductor.

Integrating Equation (3.22) over the entire conductor determines the magnetic field due to a single conductor, $H_{c,x}$:

$$H_{c,x} = \int_{-\frac{a}{2}}^{\frac{a}{2}} \int_{-\frac{a}{2}}^{\frac{a}{2}} H_{e,x} dx dy \quad (3.25)$$

This integral is evaluated numerically in MatLab using the 'dblquad' function which implements the adaptive Simpson's method for computing definite integrals.

However, the geometry of the coil includes many conductors along the x -axis. Superposition of many conductors determines the entire x component of the magnetic field, $H_{gap,x}$:

$$H_{gap,x} = \sum_1^n H_{c,x} \quad (3.26)$$

where n is the number of conductors (i.e., the coil turn count) [20]. $H_{gap,x}$ can now be substituted into the relationship for magnetic pressure, Equation (3.20).

3.2.4 MECHANICAL THEORY

Applying the magnetic pressure to the workpiece, Newton's second law is used to predict rigid body motion of the workpiece. Assuming rigid body motion of the workpiece greatly simplifies the model, and will be verified in a later section.

Incremental changes in acceleration, velocity and position are calculated, so the magnetic pressure can be recalculated as the sheet changes position. This is important since the magnetic field depends on the gap distance between the coil and the workpiece. In this way, the electromagnetic-mechanical problem is solved in a loosely coupled manner, as was represented in Figure 3.3.

Applying Newton's second law to the workpiece of mass, m :

$$\sum F(t) = mA(t) \quad (3.27)$$

where the sum of the forces, $\sum F$, is magnetic pressure exerted on the area of the workpiece, and A is the acceleration of the workpiece. The pressure distribution across the width of the workpiece is averaged and applied to the surface. Since the area that P_m acts on is also in the workpiece volume term, the area terms cancel. So applying Newton's second law and solving for acceleration, A , of the workpiece gives:

$$A(t) = \frac{\text{mean}(P_m)}{w_h \rho_w} \quad (3.28)$$

where w_h and ρ_w are the sheet thickness and density, respectively. The integration of $A(t)$ with time yields velocity:

$$V(t) = \int_{t_1}^{t_2} A dt + V_0 \quad (3.29)$$

where V_0 is the initial velocity. The integration of $V(t)$ yields the position with respect to time:

$$y(t) = \int_{t_1}^{t_2} V dt + y_0 \quad (3.30)$$

where y_0 is the initial position. The incremental change in position of the workpiece is then used to calculate a new magnetic pressure to apply.

The workpiece is initially at rest at $t = 0$, so the initial conditions for velocity and position are:

$$V(0) = 0, \quad y(0) = g_0 \quad (3.31)$$

where g_0 is the initial gap between the coil and workpiece. This gap is required for electrical insulation.

3.2.5 AERODYNAMIC EFFECTS

Two aerodynamic effects, the pressure drag on the workpiece and the aerodynamic added mass are considered to determine their effects, if any, on the workpiece velocity. Their respective magnitudes are compared to the workpiece acceleration process.

The force, F_d , due to aerodynamic pressure drag in steady flow acting on a bluff body, e.g., a flat sheet is:

$$F_d = \frac{1}{2} C_d \rho_d V^2 A_d \quad (3.32)$$

where ρ_d is the fluid density, V is the fluid (i.e., air) velocity, A_d is the cross sectional area of the plate normal to the flow direction, and C_d is the drag coefficient. The relative velocity of the workpiece to the stationary air is used as the velocity, V , in this case.

Taking compressibility into account, the drag coefficient for a square plate, C_d , is found from [22]:

$$C_d = 1.13 + .85(1 + .25M^2) \quad (3.33)$$

where M is the Mach number. The Mach number is a measure of the effect of compressibility of the fluid, and is defined as:

$$M = \frac{V}{c} \quad (3.34)$$

where c is the speed of sound in the fluid. The area of the plate is used to find the pressure applied and is compared to the magnetic pressure to determine whether this effect can safely be neglected.

As a second method for including aerodynamic effects in this model, added mass is used to approximate the inertial response of the air. This process takes the volume of space entrained by the workpiece as it is displaced and adds the equivalent mass of air to the mass of the workpiece [23]. Since the mechanical calculation is solved in a loosely coupled manner, the displacement at each step can be used to add mass to the workpiece.

3.2.6 STRUCTURAL & ELECTRICAL DESIGN

While the analytical model described above can develop the theoretically optimal coil geometry, a robust design is limited to mechanical and electrical requirements. For example, high voltages in the EMF process require space for insulation, and the mechanical loads on the coil from accelerating the workpiece require additional support.

Voltage potentials are generated between each turn of the coil from the transient current, as well as between the coil and surrounding return path. This requires adequate spacing for insulation, which was determined from the thickness and dielectric strength of the insulator. Assuming a linear relationship, the required spacing, b_s , is found from:

$$b_s = \frac{e}{d} \quad (3.35)$$

where d is the dielectric strength of the insulator, and e is the voltage potential that is being insulated.

The coil must withstand the forces used to accelerate the sheet, as well as forces generated by the coil on itself. A static mechanical FE simulation was performed in SolidWorks to estimate the stresses and deflections of the coil geometry loaded by a simplified case of the magnetic pressure predicted in the analytical model.

The loading for the FE analysis was the magnetic pressure generated from the workpiece interaction. Other forces are generated by the coil on itself, but were not included for simplicity. An attractive force exists between each of the parallel

sections of the coil, where current is flowing in the same direction. Since this would create a compressive force on the insulation, it would not likely lead to failure, but could contribute to failure stresses. Additionally, a repulsive force exists in each turn itself across the coil where current is flowing in the opposite direction. Due to the greater distance, this is a weaker force than that of the workpiece magnetic pressure, and acts in the opposite direction.

3.3 MODEL RESULTS FOR COIL DESIGN

The final coil design was driven by the analytical model initially, where an efficient design for the coil geometry to achieve maximum forming pressure or maximum workpiece velocity was predicted. However, coil designs were also limited by electrical and mechanical requirements.

3.3.1 ANALYTICAL MODEL

Results from the analytical model are presented here, which include electrical, magnetic, and mechanical predictions. These results are those of the final coil design, before any modifications are made based on experimental results (e.g., tuning coil resistance and inductance parameters from an experimentally measured primary current). Additionally, a 1mm thick, Al 6061-T6 workpiece is assumed in the analysis results.

Electrical analysis determines the electrical parameters of the final coil geometry, and the electrical response of the EMF machine and coil circuit. The EMF machine and coil parameters are shown in Table 3.1.

Table 3.1: EMF machine and coil parameters.

Machine Parameters	
Inductance (μH)	0.1
Capacitance (μF)	360
Resistance ($m\Omega$)	4.4
Coil Parameters	
Inductance (μH)	0.9
Resistance ($m\Omega$)	1.2

For the Aluminum 6061-T6 workpiece, the skin depth was 1.1mm. The predicted circuit response at 100% energy for the Maxwell Magneform 7000 JA is shown in Figure 3.7, with key response parameters shown in Table 3.2.

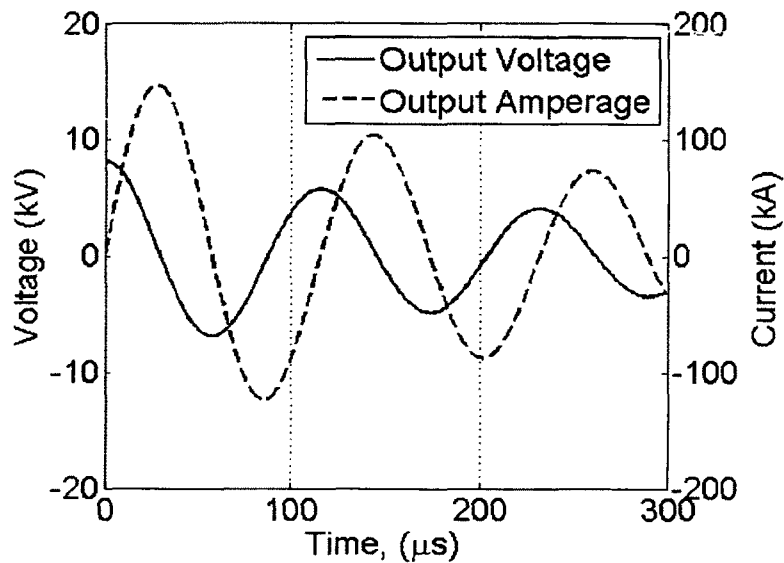


Figure 3.7: Predicted current and voltage, showing the half cycle time.

The magnetic and mechanical analysis predicts the magnetic field between the coil and workpiece, the pressure exerted on the workpiece, and the workpiece velocity. The mean magnetic pressure across the workpiece and the workpiece velocity are shown in Figure 3.8, and key parameters are also shown in Table 3.2.

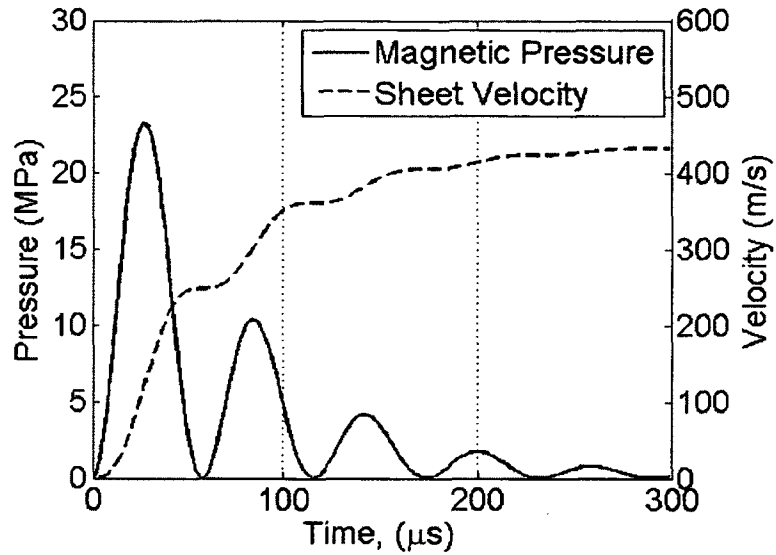


Figure 3.8: Predicted magnetic pressure and workpiece velocity.

Table 3.2: Key magnetic and mechanical response parameters.

Machine Parameter	
Energy (<i>kJ</i> (% of total))	12 (100%)
Response Parameters	
Peak Current (<i>kA</i>)	146.8
Rise Time (μs)	28
Peak Pressure (<i>MPa</i>)	23.2
Peak Velocity (<i>m/s</i>)	432

The experimentally determined coupling coefficient, k , acts on the magnetic pressure prediction to correct for the infinitely conducting workpiece assumption (i.e., $\rho \rightarrow 0$). Effects of k , as well effects from the upper and lower bound magnetic analysis are shown on the magnetic pressure in Figure 3.9.

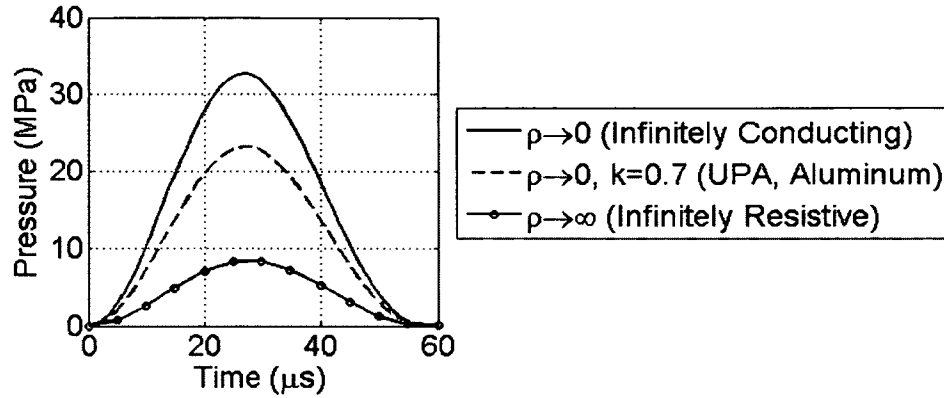


Figure 3.9: Effect of k value [9] on the predicted magnetic pressure compared to the upper and lower bound solutions [20].

3.3.2 AERODYNAMIC EFFECTS

The predicted workpiece velocity and geometric parameters listed in Table 3.4 were used to show the ratio of pressure drag to the mean magnetic pressure. As shown in Figure 3.10, the pressure drag (i.e., F_d from Equation (3.32) divided by area, A , is only significant when the magnetic pressure is temporarily zero due to the oscillating current.

To show the inertial response of the air mass during the process, the ratio of added mass to the original mass of the workpiece is presented. As shown in Figure 3.10, the added mass remains greater than two orders of magnitude smaller than the mass of the plate.

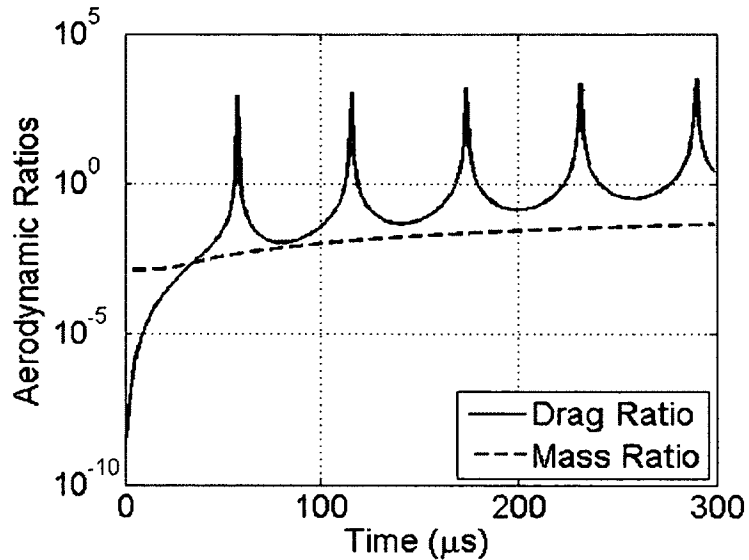


Figure 3.10: Aerodynamic effects on the workpiece acceleration, showing the drag ratio and mass ratio are more than two orders of magnitude smaller than the dominating effects.

Since the EMF/MPW process is inertially dominated, resulting velocity is sensitive to workpiece mass. Therefore, it is important to retain the aerodynamic effects if the workpiece is modified such that greater velocities are produced. Therefore, the pressure drag and added mass effects remain incorporated in the model.

3.3.3 DESIGN OPTIMIZATION

As the ratio of turns per unit length of the coil is increased, the magnetic field becomes more uniform and a uniform pressure distribution is created. This ratio can be increased by either decreasing the spacing of turns, or a decreasing the conductor width, both of which lead to a larger turn count for a given workpiece length. Since the magnetic pressure is proportional to the square of the magnetic field, the ratio of turns per unit length must be kept to a minimum. The minimum spacing is limited by the dielectric strength of the insulator, so larger dielectric

materials allow a smaller spacing, and a more uniform pressure distribution. The minimum conductor width is limited by the ability of the coil to withstand the pressure it generates. Additionally, the electrical response of the coil is greatly influenced by the coil turn count, since the inductance of the coil is proportional to the square of the turn count.

To optimize the coil for maximum sheet velocity, and thus MPW, the effect of turn count was investigated for a given coil design and workpiece length. This is important in MPW since the impact pressure that creates the weld is generated by the impact velocity. To allow for various turn counts, the conductor width was varied such that the total length of the coil equals the workpiece length. Figure 3.11 shows both predicted peak velocity and pressure during the process against the coil turn count. The pressure shown is the temporal maximum of the average pressure across the workpiece width, which occurs a different turn count than peak velocity. This is occurs since pressure (and therefore acceleration) is integrated to determine velocity.

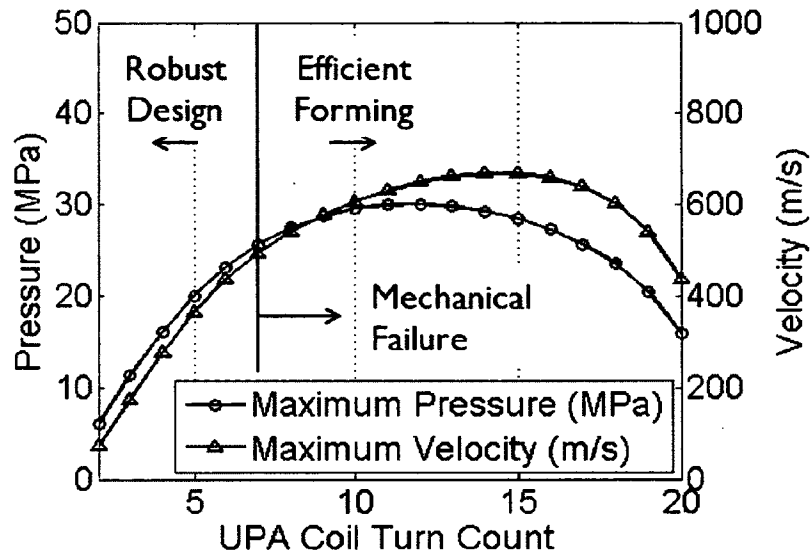


Figure 3.11: Peak pressure and velocity generated for a given turn count.

For low turn counts (e.g., less than 10 in Figure 3.11), the effect of superposition of the magnetic field from individual conductors is small, which reduces the total magnetic field strength and therefore, mean magnetic pressure across the workpiece. Although peak current is highest with a low turn count, because of the low inductance, the increase in current is not enough to compensate for the superposition effect, and results in a smaller magnetic pressure being generated.

As turn count increases, superposition of each individual conductor causes a larger total magnetic field, and magnetic pressure increases. However, a larger turn count also increases coil inductance, which produces a slower rise time and lower peak current. At a critical value for both the maximum pressure and velocity, inductance increases and peak currents are reduced to such an extent that forming efficiency is reduced from any additional turns (e.g., more than 15 in Figure 3.11).

The final design however, consists of only six turns, which is notably smaller than the optimal value for maximum velocity of 14 turns. Coil strength is the limiting factor in the design, so six turns was the maximum for the workpiece length before the coil failed the structural FE simulation. As stated previously, the pressure developed from the workpiece interaction was the only pressure included in the FE analysis since it is the most likely to cause failure. Coil strength is discussed in the following below in Section 3.4.2.

With the six turn coil, the magnetic pressure distribution was predicted along the workpiece width (x-axis in Figure 3.6). The pressure distribution varying with time is shown in Figure 3.12.

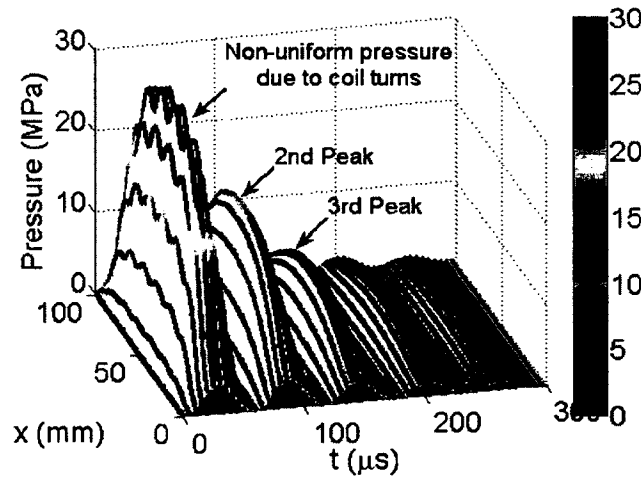


Figure 3.12: Predicted pressure distribution across workpiece width varying with time.

The pressure distribution across the workpiece is not completely uniform because of insulation requirements between the turns. The non-uniformity however, can be quantified and used in the future as input for a FE simulation to predict whether non-uniform plastic deformation would result. Additionally, the distribution becomes more uniform as the distance from the coil increases (at the

cost of a lower mean pressure), as shown in Figure 3.12 at the second and third pressure peaks.

3.4 MODEL ASSUMPTION VALIDATION

3.4.1 VERIFICATION OF RIGID BODY ASSUMPTION

Since EMF/MPW generates large plastic deformations, it is necessary to verify that the rigid body motion assumption in the mechanical analysis does not result in a loss of accuracy. A dynamic mechanical FE model was created in Dassault Systèmes Abaqus 6.11 to show that in our transient case of sheet metal forming, inertial effects dominate compared to bending forces. A workpiece thickness of 1mm and material properties of Al 6061-T6 assuming the Johnson-Cook constitutive material model were used [24]:

$$\sigma = [A = B\varepsilon^n] \left[1 + C \ln \left(\frac{\dot{\varepsilon}}{\dot{\varepsilon}_0} \right) \right] [1 - \hat{\theta}^m] \quad (3.36)$$

where σ is the effective stress, ε is the effective plastic strain, $\dot{\varepsilon}$ is the effective strain rate, $\dot{\varepsilon}_0$ is a reference strain rate, $\hat{\theta}$ is the homologous temperature, n is the work hardening exponent, and A , B , C , and m are material constants. These parameters for Al 6061-T6 are listed in Table 3.3 [24]. Simulations were stopped at strains of 100%. The mean pressure at each time step, determined in the analytical model, was applied across the entire workpiece surface. Due to the high strain rate, adiabatic heating was assumed with a inelastic heat fraction of 1.0 [24].

Table 3.3: Johnson-Cook parameters for Al-6061-T6 [24].

A (MPa)	B (MPa)	n	C	m	$\dot{\epsilon}_0$	θ_{melt} (K)	$\theta_{transition}$ (K)
324	114	.42	0.002	1.34	1	925.37	294.26

Taking advantage of symmetry, a quarter model was implemented to reduce computation time. The workpiece was fixed on one edge, to simulate the clamping force of the return path. Linear brick elements were used in the mesh shown in Figure 3.13. Element size was $0.1mm$ to $1.0mm$ with a maximum aspect ratio of 6.1, and the mesh contained 24528 elements. The workpiece dimensions were: $1mm$ thickness, $76mm$ width, and $102mm$ length. Two cases were chosen to show the effect of die radius on the rigid body assumption, i.e., die radii of $2mm$ and $10mm$. Geometric and mesh parameters are given in Table 3.4.

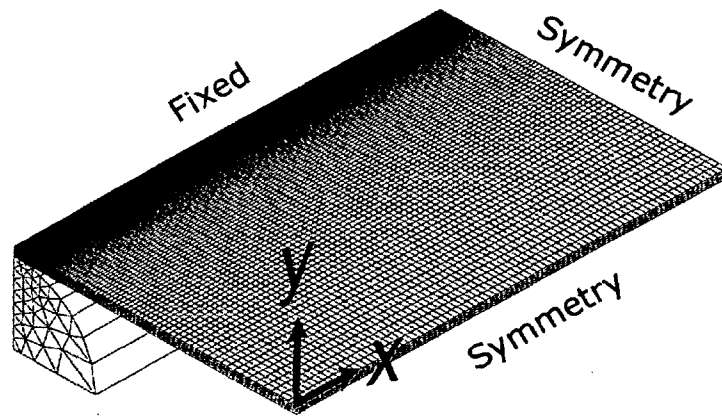


Figure 3.13: FE analysis mesh and symmetry of workpiece, with 10mm die case shown.

Table 3.4: Mechanical FE analysis parameters.

Geometric Parameters	
Workpiece Thickness (<i>mm</i>)	1
Workpiece Width (<i>mm</i>)	76
Workpiece Length (<i>mm</i>)	102
Die Radii (<i>mm</i>)	2, 10
Mesh Parameters	
Max. Element Size (<i>mm</i>)	1
Min. Element Size (<i>mm</i>)	0.1
Max Aspect Ratio	6.1
Total Elements	24528

Velocity of the workpiece was compared at the center of the sheet, where it is least affected by the clamped edge conditions. Decreasing the die radius increased the stress concentration at the edge of the sheet, and excessive strains were generated earlier in the forming event. However, for both die radii in the FE simulations, the velocity matches almost exactly with the data from the analytical model as shown in Figure 3.14. Therefore, the FE simulation validates the rigid body motion assumption at the center of the sheet in the analytical model.

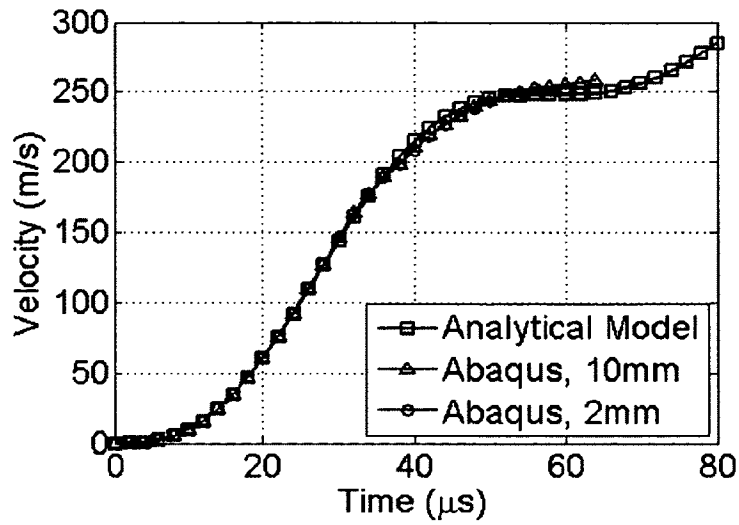


Figure 3.14: Dynamic FEA comparison for center workpiece velocity with two die radii values.

To determine if the rigid body assumption holds over the length of the workpiece, a deformed plot with resultant velocity is shown in Figure 3.15. Since the mean pressure was used as the load case, no effect of the widthwise (turn to turn) distribution is observed. This could be included with additional model complexity, but would not affect the rigid body assumption validation. The workpiece velocity is uniform except near the die region.

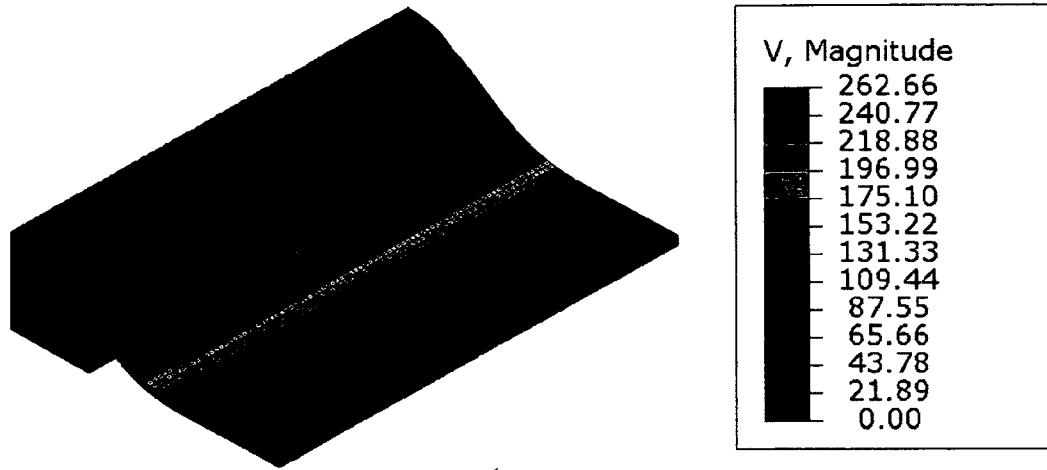


Figure 3.15: Deformed workpiece with velocity resultant vectors from dynamic FE analysis. 10mm die case shown, at time $t = 64\mu s$.

3.4.2 STRUCTURAL ANALYSIS

The coil must be designed to withstand the large forces that are generated in the process, which include the repulsive force between the coil and workpiece, the repulsive forces between each side of the coil, and the attractive forces between each turn. As with the previous sections, the results shown are that of the final coil design.

In the FEA module of SolidWorks, a static pressure was applied to the coil equal to that of the peak magnetic pressure of $29.4MPa$ as determined in the analytical model for a coil with 6 turns. To restrain the coil, a fixed boundary condition was applied to the opposite side of the coil. The coil was meshed with quadrilateral tetrahedral elements, and the coil material is UNS C18000, which is a Ni-Si-Cr-Cu alloy [25]. For a further list of FE model parameters, see Table 3.5. Since all that was of interest in this model was yielding, a linear elastic model in Solidworks was an acceptable solution.

Table 3.5: Mechanical FE analysis parameters.

Geometric Parameters	
Coil Height (<i>mm</i>)	45
Coil Width (<i>mm</i>)	95
Coil Length (<i>mm</i>)	104
Conductor Cross Section Width (<i>mm</i>)	12.3
Material Properties [25]	
Modulus (<i>GPa</i>)	130
Yield Strength (<i>MPa</i>)	607
Mesh Parameters	
Max. Element Size (<i>mm</i>)	3.2
Min. Element Size (<i>mm</i>)	1.1
Max. Aspect Ratio	4.0
Total Elements	52666

Results show that in this simplified case, the coil can withstand the forming pressure, with a safety factor of 1.32 based on the yield stress of the material. Since the repulsive force between each side of the coil is not included, this creates a conservative estimate, even with a small safety factor. See Figure 3.16 for the von Mises stress in the coil, and the locations of the boundary condition (shown in green) and applied load (shown in orange).

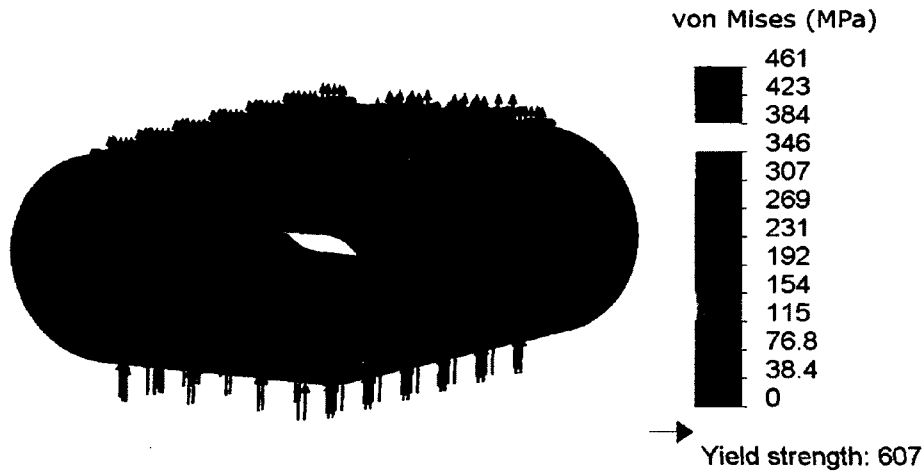


Figure 3.16: Von Mises stress from SolidWorks static mechanical FE simulation, showing fixed boundary conditions in green, and applied pressure in orange.

3.5 SUMMARY

In this chapter, analysis and design of a Uniform Pressure Actuator was presented that captures the key physics of the EMF workpiece acceleration process. Magnetic pressure developed on the workpiece, and workpiece velocities are predicted, which is useful in predicting impact velocities for MPW. Additionally, the analytical model also developed an efficient and robust design for a UPA, while maintaining its simplicity and cost effectiveness.

The analytical modeling contained electrical, electromagnetic, and mechanical stages, with assumptions and simplifications implemented to balance ease of calculation and accuracy. Aerodynamic forces are shown to a little effect on the acceleration process with the velocities predicted for typical workpieces.

However, they remain in the model since they are simple to implement, and may become significant with very thin workpieces.

Specifically, the assumption of rigid body motion was verified with dynamic, mechanical FEA which showed the inertia forces dominate in the initial acceleration process, and that bending and clamping forces have little effect. Coil strength was verified with static, mechanical FEA, and showed the coil material can withstand the magnetic reaction forces. The simplified forces applied to the coil were conservative, and allowed a safety factor on the yield stress of the material of 1.32. Further validation of the analytical model is shown experimentally with a constructed UPA in Chapter IV.

CHAPTER IV

UNIFORM PRESSURE ACTUATOR: EXPERIMENTAL VALIDATION

4.1 INTRODUCTION

The analytical model for the Uniform Pressure Actuator (UPA) described in Chapter III provides a simple and cost effective method designing a efficient coil and predicting workpiece velocities for Magnetic Pulse Welding (MPW). In this chapter, the UPA is constructed, and the analysis is verified by comparing analytical predications to experimental results. First, the electrical stage of the modeling is examined, where primary current and coil parameters are measured experimentally. Then the magnetic and mechanical stages are evaluated, where the coupling coefficient, k , and the workpiece velocity is measured experimentally. Last, the effects of workpiece thickness, conductivity, and density are investigated.

4.2 ACTUATOR CONSTRUCTION

Based on the design analysis in Chapter III, but also considering other electrical and mechanical considerations, a UPA was constructed. The actuator consists of the coil, coil leads, return channel, and epoxy potting. Clamp plates hold the assembly together and allow for mounting of sensors to measure workpiece displacement and velocity. Images of the hardware are shown in Figure 4.1a, and the following sections describe each part of the assembly.

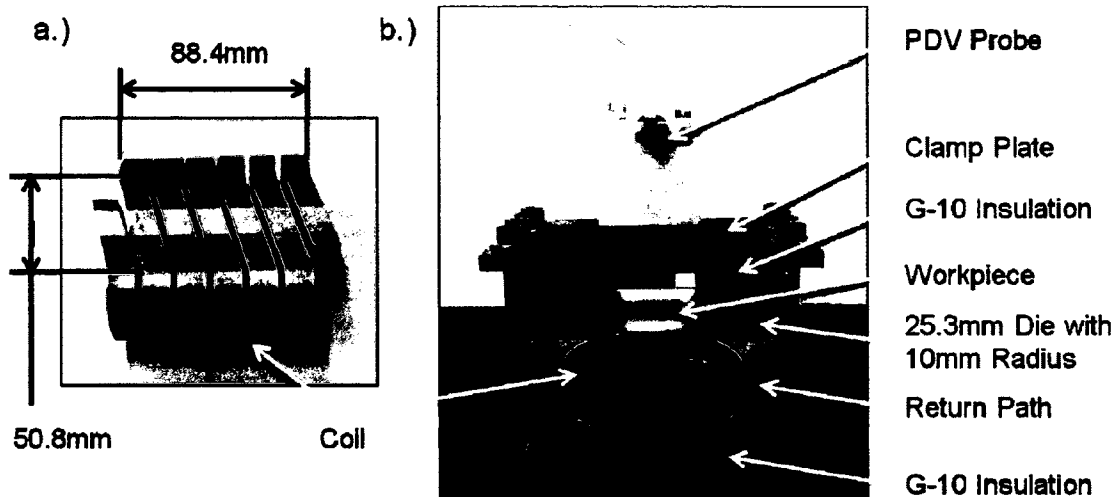


Figure 4.1: Pictures of a.) coil, and b.) the complete UPA assembly with PDV probe.

4.2.1 COIL GEOMETRY & CONSTRUCTION

The coil consists of six full turns and a spacing between each turn of 3mm . Wire Electric Discharge Machining (EDM) was used to cut the coil from a solid billet of UNS C18000 (2Ni-1Si-1Cr-96Cu) by Vaupell Rapid Solutions (Nashua, NH), shown in Figure 4.1. This high performance copper alloy was selected for its high yield strength (607MPa) and low electrical resistivity ($3.592 \times 10^{-8} \Omega \cdot \text{m}$) [25].

A deformable workpiece area of $48.1\text{mm} \times 127\text{mm}$ was selected for the UPA geometry, but the actual workpiece width is larger to contact the return path. The cross section of the conductor is $12.3\text{mm} \times 12.3\text{mm}$, which was determined in the static FE mechanical simulation to withstand the forming pressures. A dimensioned drawing is provided in Figure 4.2.

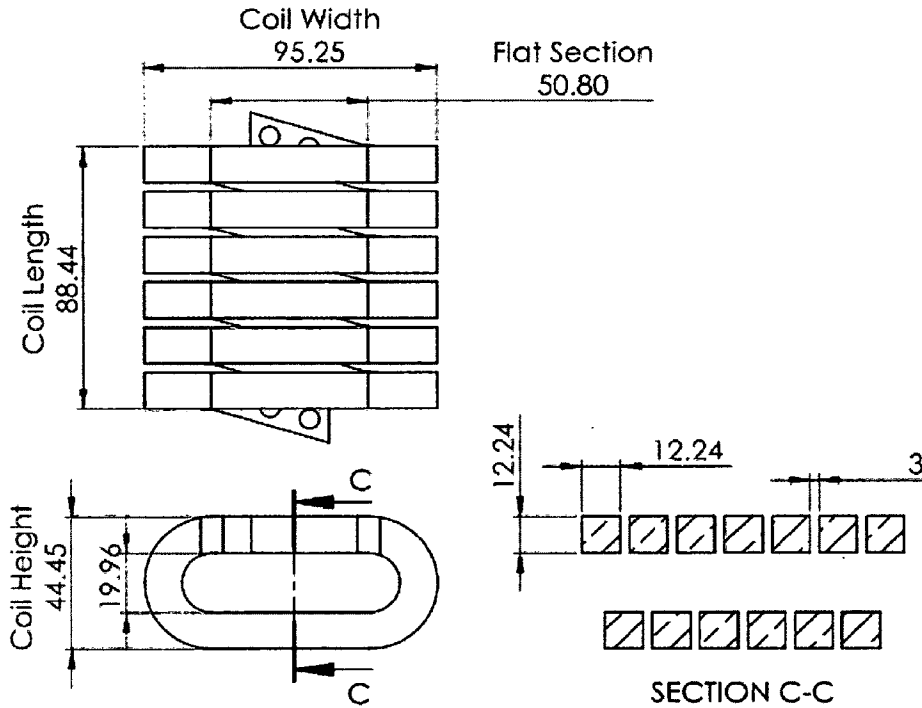


Figure 4.2: Dimensioned drawing of coil geometry (dimensions in mm).

Two Cu 110 leads extend from the coil for attachment to the capacitor bank, with a 25.4mm x 4.8mm cross section and extend 175mm from the coil. The leads were bent to accommodate connections to the capacitor bank and were attached with press fit pins to secure them during the brazing process. Since the brazing process would soften the material, a heat treatment is required after brazing to increase the strength and conductivity of the C18000 alloy. Refer to Table 4.1 for heat treatment specifications.

Brazing and heat treating of the coil and leads assembly was performed by Brazecom Industries (Weare, NH). Pure silver brazing filler metal was used, and a vacuum furnace was employed to prevent oxidation.

Table 4.1: Heat treatment specifications for UNS C18000 after brazing of leads [26].

Process	Temperature	Time
Solution Treatment	930°C	30min.
1st Aging	540°C	3hr.
2nd Aging	425°C	3hr.

4.2.2 RETURN PATH & POTTING

The return path consists of an Al-6061 T6 channel, with a 3mm gap between itself and the coil to allow for electrical insulation. The geometry of the return path allows eddy currents generated in the sheet to flow in a circuit, and its close proximity to the coil allows for further eddy current generation. This increases the forming efficiency of the coil and provides a surface to clamp the workpiece in place [9]. A dimensioned schematic is shown in Figure 4.3.

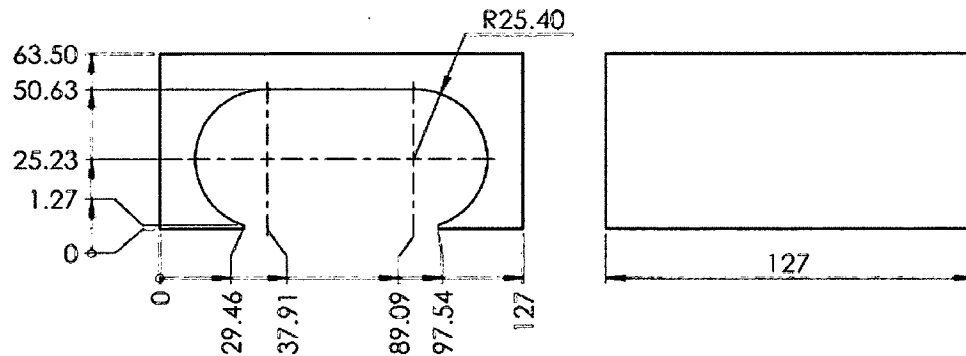


Figure 4.3: Dimensioned drawing of return path geometry (dimensions in mm).

To provide electrical insulation and support for the coil, a clear epoxy from MG Chemicals (8321C) was used to pot the coil into the return path. Transparency of the epoxy allows for visual inspection of cracking and arcing damage. Figure 4.4 shows the coil potted in the return path and the corresponding dimensions.

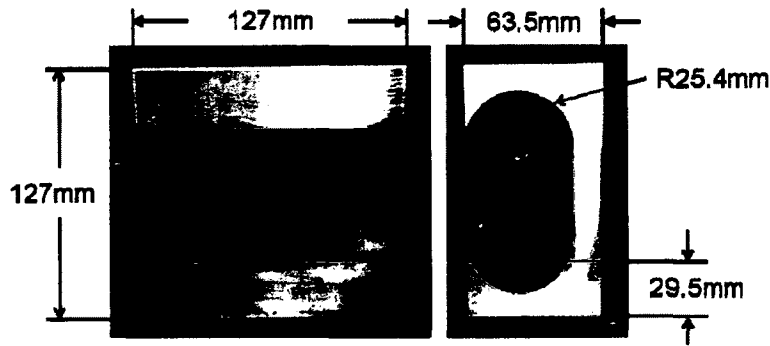


Figure 4.4: Coil potted in return path.

Steel plates and eight $3/8$ in bolts provided a clamping force between the workpiece and return path, as shown in Figure 4.1b. Phenolic G-10 sheets were inserted between the steel plates to insulate them from the high voltages produced. Free forming G-10 dies with a 25.4mm height and 10mm radius were placed under the workpiece to allow the sheet to accelerate away from the coil.

4.3 EXPERIMENTAL SETUP

Once designed and constructed, the UPA was connected to a Magneform 7000 JA series, 12kJ capacitor bank to generate the large currents necessary for EMF/MPW. Six $60\mu F$ capacitors are connected in parallel for a total of $360\mu F$, which can be charged to a maximum 8.3kV. Six coaxial cables connect the capacitors to the coil clamping mechanism at the forming box. The clamping mechanism uses four $5/8$ in. bolts to apply contact pressure to the coil leads.

A Powertek CWT 3000B Rogowski coil was implemented in the coil clamping mechanism to measure the primary circuit amperage. The Rogowski coil encircles one lead from the Magneform, (see Figure 4.5a) and a voltage is induced in it from the current in the lead. This voltage is integrated and amplified

with external circuitry. From the amplifier, a waveform is produced linearly proportional to the amperage in the lead, with a 0 – 6V output corresponding to a measurement range from 0 – 600kA.

For workpiece velocity measurements, a Photon Doppler Velocimetry (PDV) probe is implemented in the clamping fixture to observe the center of the workpiece as it deforms away from the coil (see Figure 4.5b).

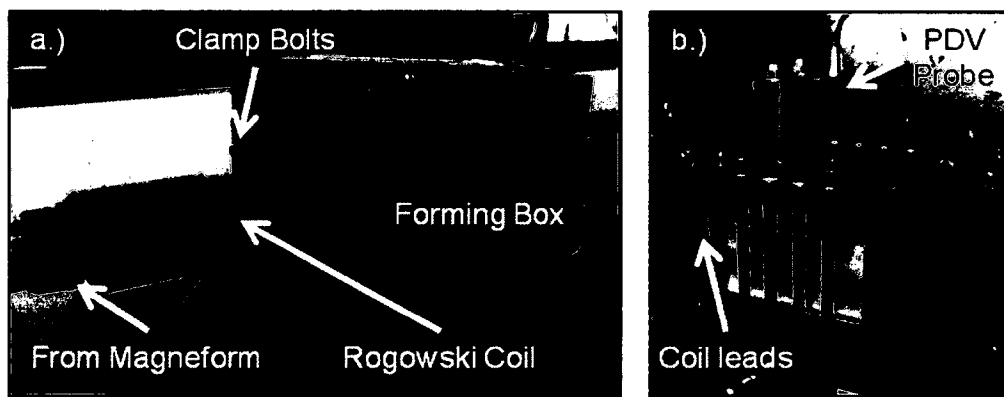


Figure 4.5: Experimental setup showing a.) the exterior and b.) the interior (i.e., in the forming box) details.

4.4 PHOTON DOPPLER VELOCIMETRY

4.4.1 OPERATING PRINCIPLES

PDV is a laser interferometric technique for measuring large target velocities.

PDV provides a robust method for measuring velocities with submicron displacement resolution and temporal resolution in the nanosecond range [27].

This technique has been previously implemented to measure workpiece velocity during MPW, and is considered a standard in high target velocity measurement techniques [1].

A laser is aligned normal to the target, which reflects off the surface with a shifted frequency. The frequency shift is proportional to the velocity of the target, which is known as the Doppler effect. When the shifted beam is mixed in a optical circulator with the original beam, a beat frequency that is also proportional to the target velocity is produced. Figure 4.6 shows a typical schematic for a PDV system.

The beat frequency is many orders of magnitude smaller, such that it is capable of being recorded by high speed optical detectors and a oscilloscope. The beat frequency, f_{beat} is determined by [27]:

$$f_{beat} = v / \left(\frac{\lambda}{2} \right) \tag{4.1}$$

where v is the target velocity, and λ is the laser wavelength.

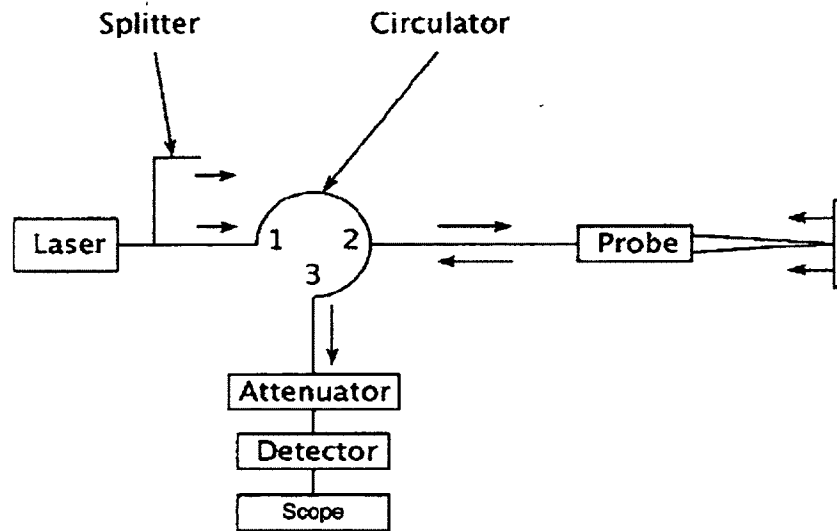


Figure 4.6: Schematic of a PDV system with target [27].

4.4.2 CAPABILITIES

The PDV system available in the author's laboratory was designed and built by the Ohio Manufacturing Institute [28]. The system is capable of measuring target velocities up to $500m/s$, at a working distance of $100mm$. A $2W$, $1550nm$ wavelength laser is split into two beams; one for each of two probes. Each probe uses a lens with a $99mm$ working distance and a displacement range of about $20mm$, centered at the working distance (although this can be extended by applying reflective tape to the target).

Maximum velocity is limited by the bandwidth of the optical detectors and the oscilloscope. The oscilloscope for this system is a LeCroy WaveSurfer 64MXs-B. With a $600MHz$ bandwidth, the oscilloscope limits the maximum velocity of the system to approximately $500m/s$.

4.4.3 CALCULATION OF VELOCITY

To determine the target velocity, we need to determine the frequency content as it changes with time in the recorded beat frequency. A short time Fourier transform (STFT) can be performed on the recorded beat frequency which provides information about both when and what frequencies occurred in the signal (i.e., a spectrogram). The STFT performs a Fourier Transform on a overlapped, windowed portion of the signal, and returns the strength of each frequency for that window in time. The maximum strength frequency is selected for each window, and the target velocity can then be found from Equation (4.1).

4.5 RESULTS

4.5.1 ELECTRICAL RESULTS

The accuracy of the electrical analysis of the model can be verified by experimental measurement of the coil parameters. Electrical parameters were determined from the response of the primary current through the circuit comprised of the pulsed power supply, leads, and coil. Before the coil parameters can be determined however, the Magneform pulsed power supply must be characterized.

The electrical parameters of both the Magneform pulsed power supply and the UPA were determined by measuring the primary circuit's response with a 3.6kJ discharge. For characterization of the Magneform, the clamping mechanism where the coil is typically located was electrically shorted. The values of the machine resistance, R_m , and the machine inductance, L_m , can be determined experimentally with a known capacitance by calculating the damped natural frequency and damping ratio of the series resistance-inductance-capacitance (RLC) circuit.

After charging the capacitor, the main switch is closed, and an exponentially decaying, sinusoidal waveform is produced. Measurements are taken of the wavelength, λ , the first positive peak amplitude, A_1 , and the n -th positive peak amplitude, A_n . With these parameters, the damped natural frequency, ω_d , is determined from Equation (3.10), and L_m and R_m are determined from Equation (3.11) and (3.12) respectively. For the Magneform with $C = 360\mu\text{F}$, the experimentally determined parameters are $R_m = 4.4\text{m}\Omega$ and $L_m = 0.1\mu\text{H}$.

The electrical parameters of the UPA were to determined in a similar manner, since the coil resistance, R_c , and coil inductance, L_c , adds in series with the Magneform circuit. Therefore, $R_c = R - R_m$ and $L_c = L - L_m$, where R and L are the total resistance and inductance measured in Magneform-UPA circuit. A 1mm Al-6061-T6 workpiece was formed with the UPA connected to the Magneform, and a 3.6kJ (30%) discharge was applied. Current measured with the Rogowski coil is shown in Figure 4.7, with a predicted discharge using the experimentally measured circuit parameters.

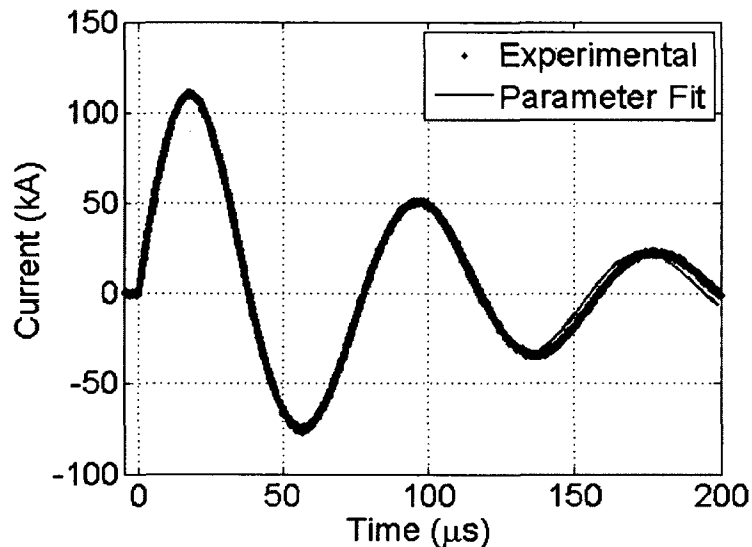


Figure 4.7: Experimental fit to current waveform during a 3.6kJ discharge and 1mm Al-6061-T6.

Figure 4.7 shows the experimentally measured response varies slightly from the second order RLC response later in the forming process. This is due to deformation of the workpiece, which slightly changes the circuit parameters [12]. The experimentally determined electrical parameters are compared to the predicted parameters from the analytical model in Figure 4.8.

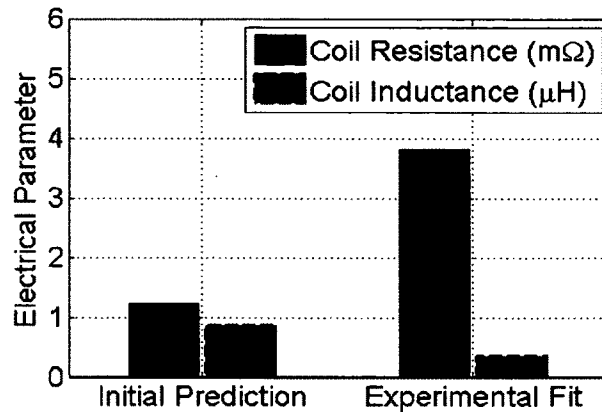


Figure 4.8: Comparison of initially predicted and experimental electrical parameters. The experimentally measured electrical response of the UPA showed the coil's inductance is smaller than the analytical prediction. This is expected since the return path and workpiece which are not included in the calculation act to shield the magnetic field around the coil. This reduction area that the magnetic field is contained in reduces the inductance of the coil [12]. The predicted resistance is significantly smaller than the experimentally measured resistance, which could be due to a change in the coil material's resistivity during the heat treatment, or possibly from the added resistance from the brazed joints in the coil. While the relative error in electrical parameter prediction appears large, it was still sufficiently to reasonably predict velocities accurately (see Figure 4.9).

The predictions of current through the coil and workpiece velocity are based of coil inductance and resistance values, so any error in these parameters propagate through the analytical model. To show extent of the parameters prediction error and the models sensitivity to this error, peak current and maximum velocity for both sets of electrical parameters are shown in Figure 4.9.

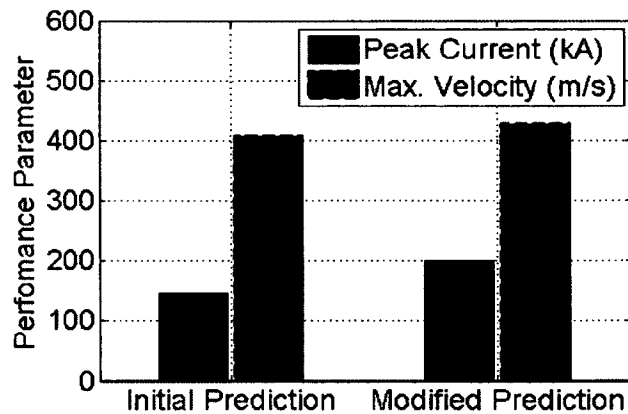


Figure 4.9: Electrical parameters' error on analytical model output of peak current and maximum velocity.

While the relative error in electrical parameter prediction appears large, it was still sufficiently accurate to predict velocities accurately, which is the purpose of the modeling.

4.5.2 COUPLING COEFFICIENT

In Chapter III, a coupling coefficient was introduced in the magnetic stage of the model to account for the simplification that the workpiece was assumed to be superconducting. This simplification over-predicts the magnetic field produced in the coil-workpiece gap region, so a coupling coefficient was included which can range from $0 \leq k \leq 1$ [9,21]. Alternatively, if the coil and workpiece are considered a transformer with imperfect coupling, the coupling coefficient can be thought of as modifying the ratio between the primary current and the induced current. Both currents can be measured experimentally to provide a direct measurement k from Equation (3.21).

A slightly modified experimental setup was necessary for measurement of the induced current in the workpiece. A 1mm 6061-T6 workpiece was manually

deformed to create a small channel for the Rogowski coil to surround the workpiece. Photographs of this experimental setup are shown in Figure 4.10. Measurements of the primary and induced currents were recorded with this setup and a 3.6kJ discharge. Higher energy tests were not performed due to concerns of deforming the workpiece and damaging the Rogowski coil. The average of three experiments shown in Figure 4.11, with bars representing the range of values from the three experiments.

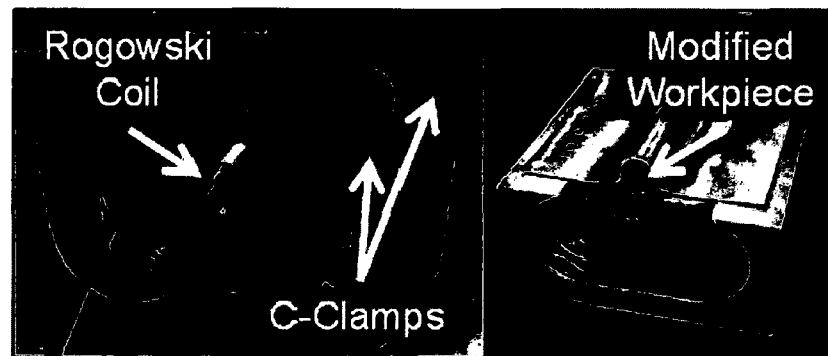


Figure 4.10: Modified experimental setup for measuring induced current in workpiece.

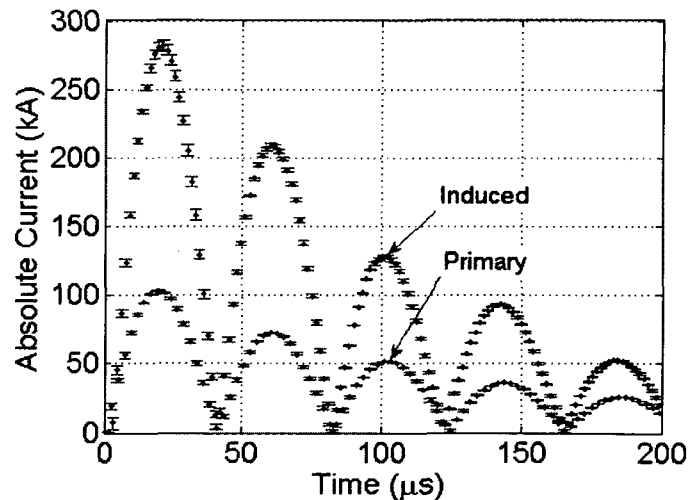


Figure 4.11: Primary and induced currents in the coil and workpiece.

From the ratios of the primary and induced currents, a best fit with the least squares method was used with Equation (3.21) to determine $k = 0.45$. This is in

contrast to Kamal's $k = 0.70$ for a UPA and Aluminum workpiece. They termed the parameter f_2 , and in their experimental setup the Rogowski coil passed through the coil, such that a artificially deformed workpiece was not necessary. Alternatively, Xu et al. determined $k = 0.09$ for Aluminum. They termed the parameter λ , which was equivalent to $k^{1/2}$ since is acted on H_{gap} rather than P_m . This however was for a flat spiral coil with no return path [21], which is known to be less efficient with respect to inducing eddy currents in the workpiece.

To show the sensitivity that k has on predicting workpiece velocities, the analytical model was rerun with $k = 0.35$ and $k = 0.55$. A 1mm 6061-T6 workpiece was used with a 6kJ discharge. The velocities are shown with $k = 0.45$ in Figure 4.12.

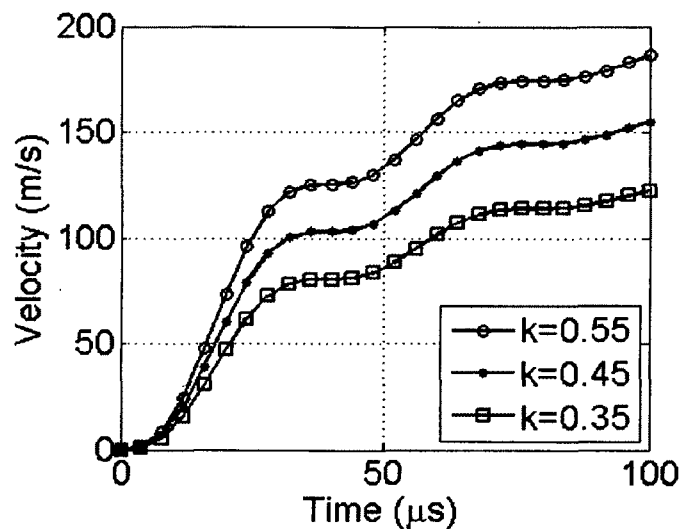


Figure 4.12: Predicted velocities for varying k , with a 6kJ discharge and 1mm 6061-T6 workpiece.

4.5.3 VARYING DISCHARGE ENERGY

To verify the analytical model in Part I for workpiece velocity prediction, three energy levels of 3.6kJ , 6kJ , and 8.4kJ were used to accelerate and deform 1mm thick 6061-T6 workpieces (see Figure 4.13). The analytical model predictions shown are those with the modified electrical parameters (see Figure 4.8a) and $k = .45$. Experiments were repeated three times at each energy level, with the average shown in Figure 4.13. The bars represent the range of values from the three experiments.

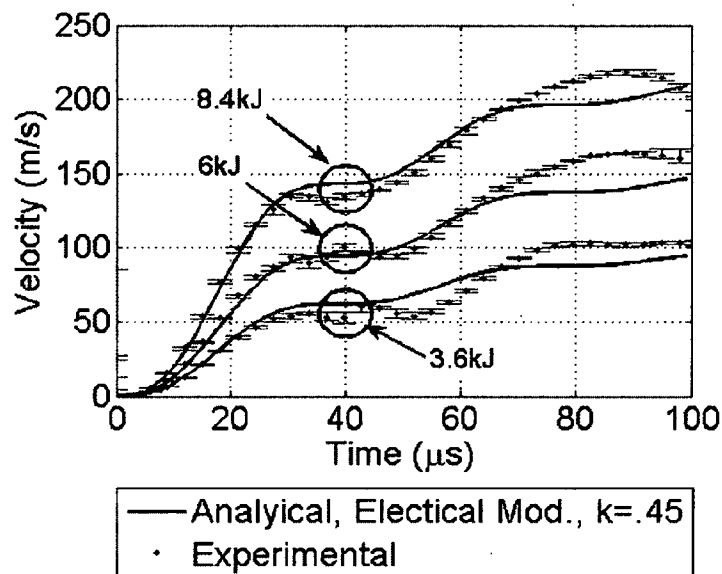


Figure 4.13: Experimental velocity results from a 3.6kJ , 6kJ , and 8.4kJ discharge and 1mm Al 6061-T6 sheets, with the analytical model predictions shown for comparison.

The analytical model is shown to accurately predict workpiece velocity during the initial acceleration, up to approximately the first plateau in velocity. However, the model is limited in the inability to predict velocity later in the forming process, as the rigid body motion assumption is invalidated and bending forces overcome the inertial forces in the workpiece.

Photographs of the deformed workpieces are shown in Figure 4.14 for the three energy levels. The side view in Figure 4.14b shows the relative uniformity of the deformation across the six turns of the coil, which is where the UPA gains its name. Some increased deformation is observed on the outer edges of the workpiece in Figure 4.14b, which is due to increased current density on the edge from the skin effect [29].

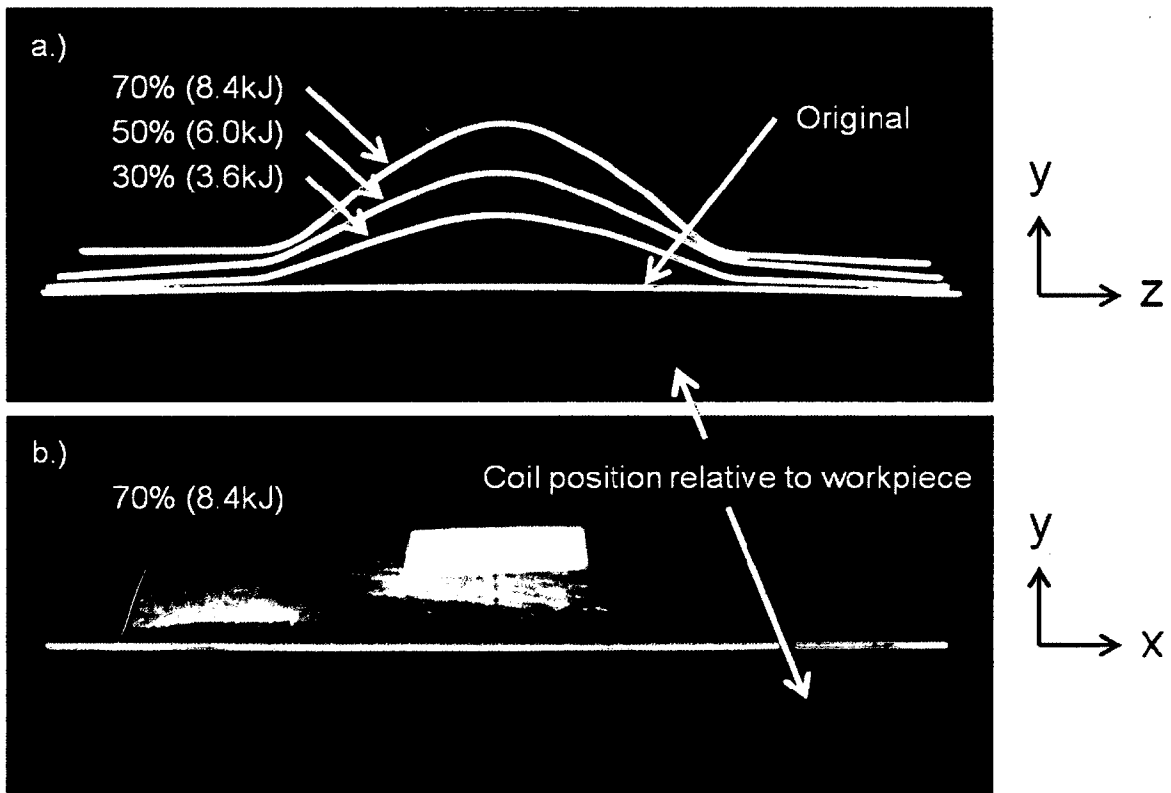


Figure 4.14: Deformed 1mm 6061-T6 workpieces from a 3.6kJ, 6kJ, and 8.4kJ discharge energies, showing a.) front view (i.e., view normal to coil axis) and b.) side view (i.e., coil turns across photograph).

4.5.4 VARYING THICKNESS

If the skin depth in the workpiece (Equation (3.3)) is large compared to the workpiece thickness, the magnetic field will penetrate through the thickness, and less magnetic pressure will be developed. In the analytical model, an assumption

was made that the magnetic field does not penetrate completely through the workpiece, due to the skin effect. This allowed a straightforward determination of the magnetic pressure acting on the workpiece.

For this simplification to be valid however, it was recommended by past researchers that the ratio of workpiece thickness to skin depth, α , should be at least 1.5 to 2.0 [1]. In order to verify this assumption for our experimental case, a series of forming tests was performed with the UPA, while varying the α ratio by changing the thickness of the workpiece. The skin depth remains constant since it is material, not thickness dependant. Al-6061-T6 sheets where formed with a $6kJ$ discharge. The thickness and corresponding α ratio are listed in Table 4.2.

Table 4.2: Various workpiece thickness and α ratios with a skin depth of $\delta = 1.2mm$.

Thickness	α
0.5mm	0.57
1mm	1.1
2mm	2.3

At the ringing frequency of the discharge circuit, Al-6061-T6 has a skin depth of $\delta = 1.2mm$. Velocity results for the average of three experiments at each thickness were measured with PDV are shown in Figure 4.15. The bars represent the range of values from the three experiments. The corresponding analytical predictions with the modified electrical parameters and $k = .45$ are also shown in Figure 4.15 for comparison.

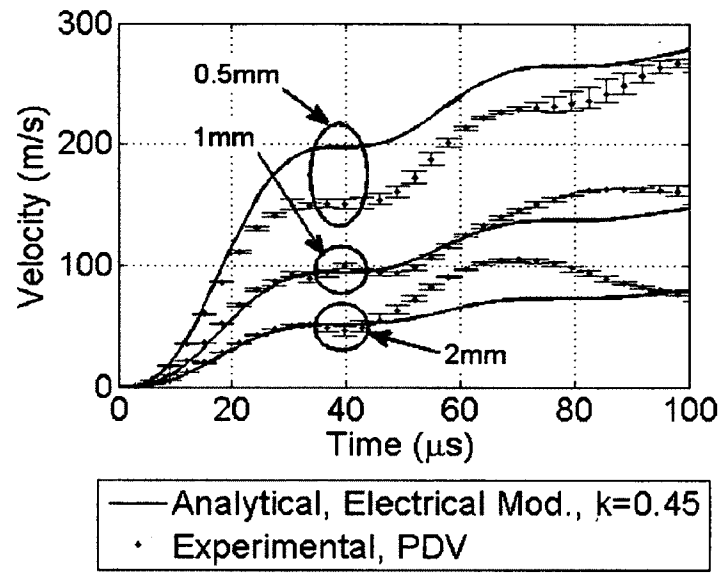


Figure 4.15: Workpiece velocity with varying workpiece thicknesses and analytical model prediction. Discharge energy was 6kJ.

The 1mm and 2mm thicknesses show no change from the analytical model during the initial acceleration. Therefore, even a α ratio as low as $\alpha = 1.1$ is acceptable for determining the magnetic pressure with the aforementioned assumption. This is lower than the α ratio of 1.5 to 2.0 recommended in past research, which is useful for predicting thinner workpiece velocities. This also shows that the magnetic coupling (and therefore, k) remains constant above some critical value of α . The $\alpha = 0.57$ experiment produce a slower velocity from the analytical prediction, which demonstrates that smaller α ratios do not fully contain the magnetic field, and thus the forming pressure are velocity are reduced.

4.5.5 VARYING MATERIAL CONDUCTIVITY

The coupling coefficient, k , was measured experimentally with an Aluminum workpiece, however, the magnetic coupling may change with workpiece

conductivity, since the skin depth depends on conductivity. For example, previous research with a UPA showed a coupling coefficient of $k = 0.70$ for Aluminum, and $k = 0.55$ for stainless steel (having resistivity's of $5.9\mu\Omega cm$ and $69.5\mu\Omega cm$ respectively) [9]. However, $\alpha = .57$ for the Aluminum workpiece, and $\alpha = .15$ for the stainless steel workpiece in their experimental setup. Therefore, the difference in k can be attributed to low α ratios.

To show that magnetic coupling is not material dependent for α greater than some critical value, two other materials were formed with the UPA, and their velocities were compared to the analytical prediction with $k = .45$ to observe any significant difference. Materials with conductivities both higher and lower than Aluminum 6061-T6 were chosen. The alloys and their material properties are listed in Table 4.3. All workpieces were $1mm$ in thickness. Each material was formed three times, with a $6kJ$ discharge, and the average velocity values measured with PDV are shown in Figure 4.16 along with the analytical model prediction with $k = .45$. The bars represent the range of values from the three experiments.

Table 4.3: Material properties for workpiece conductivity experiments.

Material	Resistivity (Ωm)	Conductivity (% IACS)	Density (kg/m^3)	α
Cu 110	1.72×10^{-8}	100	8890	1.7
Al 6061-T6	3.99×10^{-8}	43	2660	1.1
Cu 230	6.15×10^{-8}	27	8530	0.91
Cu 510	11.9×10^{-8}	15	8860	0.66
SS 321	72×10^{-8}	2.4	8000	0.27

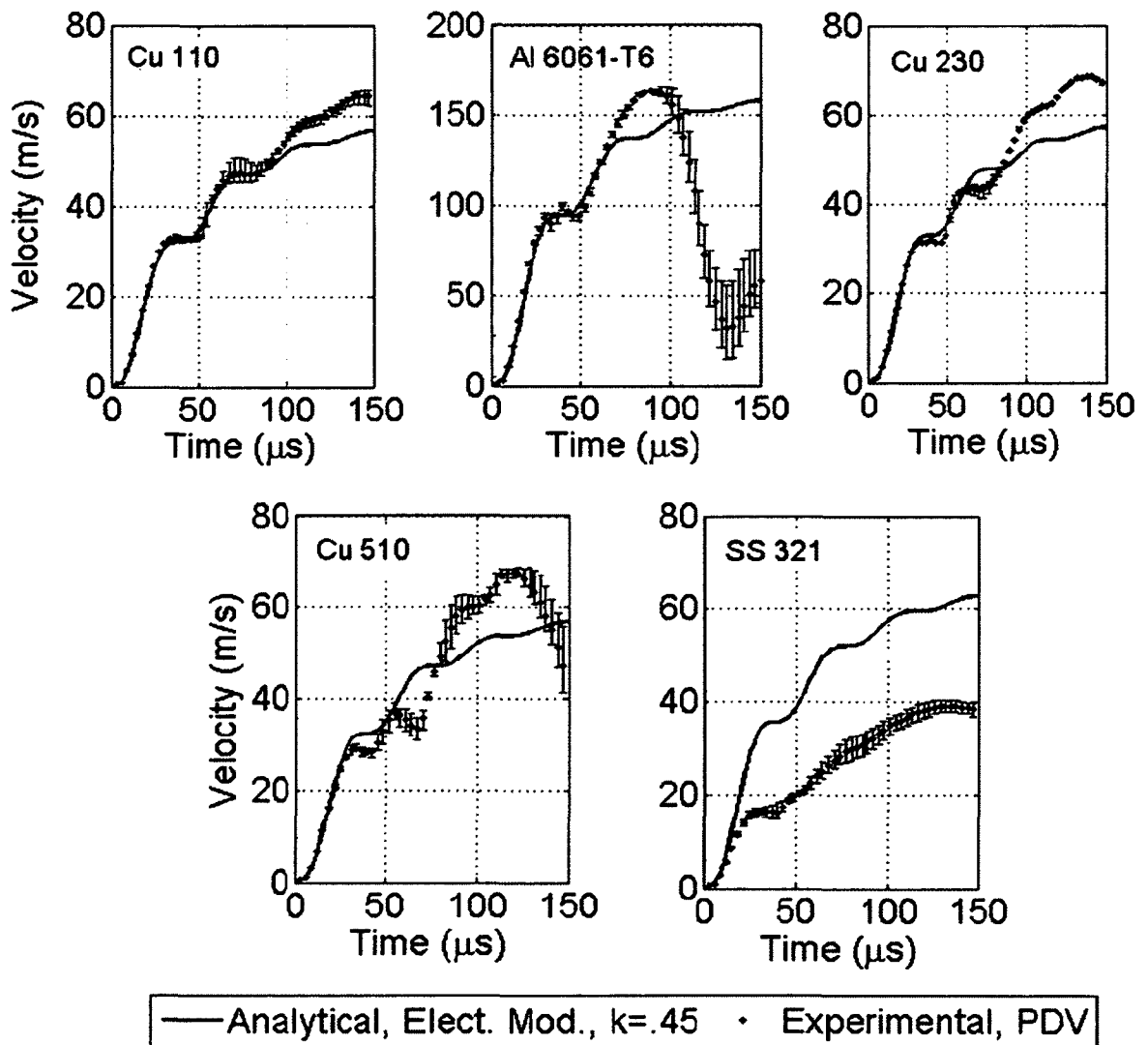


Figure 4.16: Workpiece velocity with varying workpiece conductivity and analytical model prediction. Discharge energy was 6kJ.

Results show accurate velocity prediction during the initial acceleration with $\alpha > 0.66$, which shows that the magnetic coupling is constant when varying the workpiece material above a critical α ratio. However, the measured velocity is lower than predicted for the stainless steel experiment, where $\alpha = 0.27$. Since the materials also have large differences in densities, this series of experiments also shows that rigid body motion captures the initial acceleration well, and that the acceleration process is highly dependent on inertial forces. For example, with the lighter Aluminum, the velocity decreases rapidly in the later part of the forming process due to decreased inertial forces.

4.6 SUMMARY

In this chapter, a UPA was constructed based on the analytical model presented in Chapter III. Electrical parameters of a commercial Magneform pulsed power supply and the constructed UPA were measured and compared to analytical predictions. Electrical parameter prediction was shown to have sufficient accuracy for the purpose of predicting workpiece velocities. Experimental measurement of the magnetic coupling coefficient, k , was performed and $k = 0.45$ for our UPA.

Measurements of the workpiece velocity for various energy levels was performed, with the analytical model showing a high level of accuracy with the experimentally determined electrical parameters and $k = 0.45$. The workpiece thickness to skin depth ratio, α , was investigated experimentally to observe its effects on the magnetic coupling. The α ratio was first varied by changing the

workpiece thickness. The analytical model predicted workpiece velocity accurately for $\alpha > 1.1$, but decreased coupling was observed for $\alpha = 0.57$. The α ratio was then varied by changing the workpiece resistivity. The analytical model predicted workpiece velocity accurately for $\alpha > 0.66$ but decreased coupling was observed for $\alpha = 0.27$.

CHAPTER V

FIBER OPTIC DISPLACEMENT SENSOR

5.1 INTRODUCTION

PDV was implemented in the UPA for workpiece velocity measurement, which is considered a standard in high target velocity measurement techniques [1].

However, the system is expensive and contains a Class IV laser which requires additional safety precautions. As an alternative workpiece velocity measurement technique, a fiber optic displacement sensor was investigated. Compared to a PDV system, the fiber optic sensor is less expensive by a factor of 20, safer, and similar in ease of implementation.

The fiber optic, reflectance-based sensor used in this research was a Philtec D63-C6H2T3 with an included analog amplifier (see Figure 5.1: for a schematic of the sensor). Therefore, displacement resolution is only limited by the analog to digital converter of the data acquisition system. The $-3dB$ bandwidth of the amplifier is $2MHz$, and the amplifier output is a $0 - 5V$ signal proportional to displacement. A $3.2mm$ ($0.125in$) nonconductive sensor tip provides electrical isolation, and the beam angle is 66° . The displacement range for mill-finish aluminum is approximately $3mm$, but in this research this parameter was extended to $27mm$ with the use of reflective tape. PDV systems are not limited in

displacement ranges, so it may be necessary to implement PDV in large displacement applications.

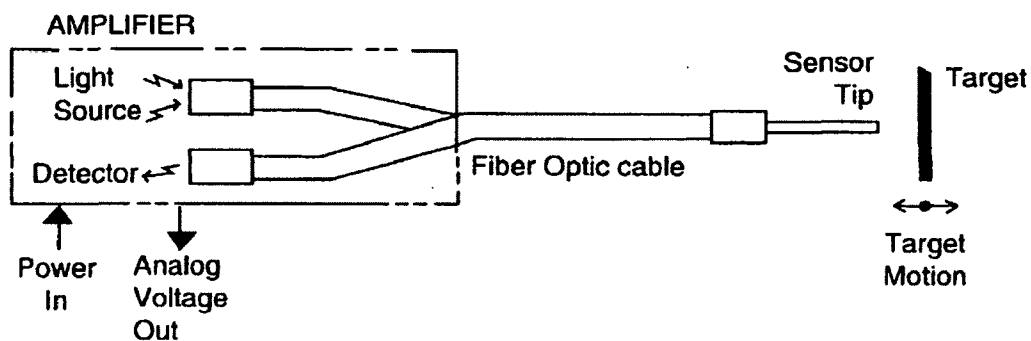


Figure 5.1: Reflectance dependant, fiber optic sensor operation schematic [30].

5.2 SENSOR CHARACTERIZATION

5.2.1 LINEAR AND ANGULAR DISPLACEMENT

Some limitations exist for the fiber optic sensor. Since displacement is correlated to the reflected light intensity, any change in surface reflectivity, alignment, or curvature produces an apparent displacement which cannot be discerned from the normal translation of interest. Therefore, the sensor response was characterized for surface misalignment, curvature, and reflectivity values observed in EMF and MPW.

In order to characterize the fiber optic sensor for possible surface effects during high velocity EMF and MPW multiple tests and experiments were performed. Many of the tests describe effects from incidence angle, i.e., the difference between a surface and the line normal to that surface. This angle is of interest in impact processes such as MPW; however, it is not possible to discern a change in incidence angle (which may occur during deformation) from translation.

For simplicity, the sensor characterization tests are performed as static calibrations. A two axis translation stage was used for movement in the normal and tangential directions, as shown in Figure 5.2.

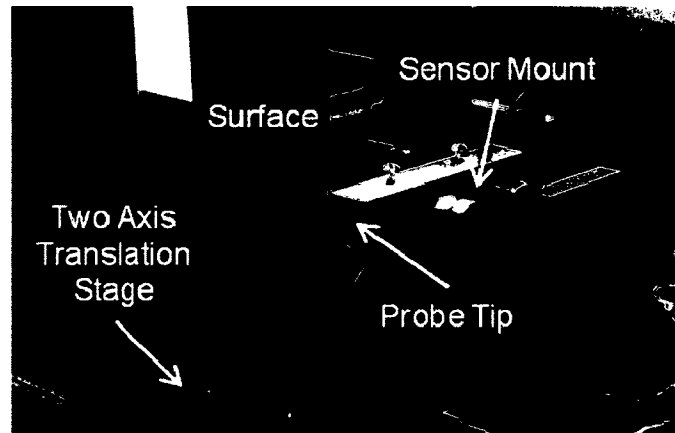


Figure 5.2: Experimental setup for sensor characterization.

A calibration curve for translation from a flat, mill-finish aluminum surface was obtained. The surface was then displaced from the sensor and a voltage reading was taken at each 0.0254 mm (0.001 in) distance increment. The calibration curve is shown in Figure 5.3.

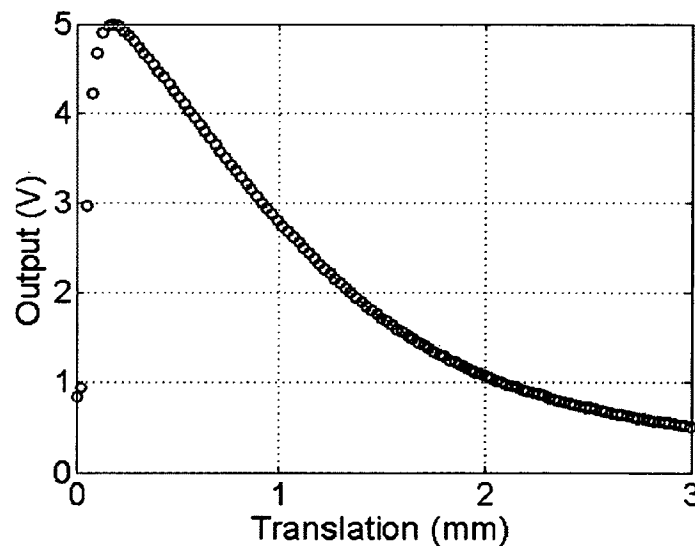


Figure 5.3: Calibration curve for flat, mill-finish aluminum surface.

There is a peak in sensor output at 0.2 mm (0.008 in) due to near field effects. Therefore, in order to eliminate ambiguity, only the displacement range contained in the far-field ($> 0.2 \text{ mm}$) was used. This represents the initial stand-off distance from the target if the target is moving away from the sensor.

Angular effects were investigated for flat sheet and axisymmetric EMF processes. A flat, mill-finish aluminum surface and two mill-finish aluminum cylinders were used as target surfaces as they were either rotated or displaced. Angular changes for the flat surface (Figure 5.4a) and the horizontal cylinder (Figure 5.4b) were achieved using a rotating stage, and translational changes on a vertical cylinder were achieved using a two axis translation stage (Figure 5.4c).

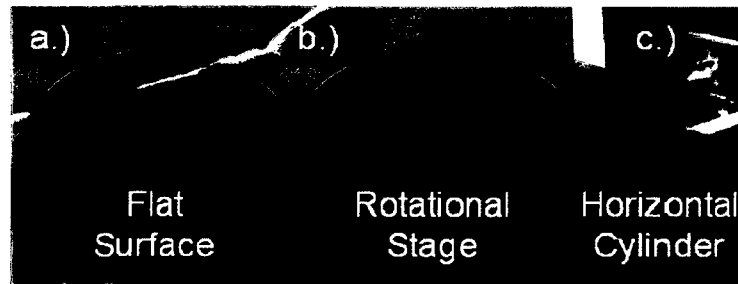


Figure 5.4: Experimental setups for angular effects: a.) flat surface, b.) horizontal Cylinder, and c.) vertical cylinder.

For the flat surface and the horizontal cylinder, the sensor was located 1 mm (0.039 in) from the surface. The surface was then rotated using the rotational stage in one degree increments between $\pm 7^\circ$. The sensor outputs were converted to gap distance values using the calibration curve and compared with the actual gap to compute an error from misalignment, shown in Figure 5.5.

For the vertical cylinder, the two axis translation stage was used to traverse the fiber optic sensor location across the diameter. The theoretical gap distance and

incident angle were calculated for a circular geometry. The sensor outputs were converted to gap distance values using the calibration curve (Figure 5.3) and compared with the theoretical gap to compute an error from misalignment, also shown in Figure 5.5.

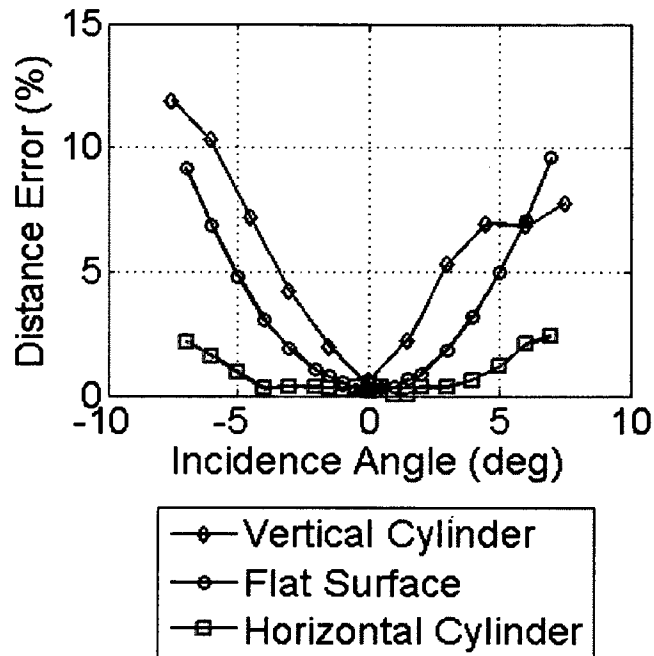


Figure 5.5: Gap distance error induced from angular effects for three experiments: flat surface, horizontal cylinder, and vertical cylinder.

Based on the complex geometry of the work pieces that were used in EMF processes, the horizontally oriented cylinder will help to quantify the error during tube/shaft EMF. For flat sheet EMF, the flat surface tests will help to quantify possible error.

As is evident in Figure 5.5, an increasingly large error occurs with increasing incidence angles for all three surfaces. Also, the working range for the sensor is relatively small ($< 3mm$). Finally, while not shown here, the surface roughness affects output values from the fiber optic sensor.

5.2.2 RETROREFLECTIVE SURFACE

These limitations of the fiber optic sensor, i.e., large errors at small incident angles and sensitivity to surface roughness, can be alleviated with the use of retroreflective tape. Retroreflective surfaces, popular on roadway signs and markings, reflect light back to the light source, which is advantageous for minimizing changes in surface reflectivity due to roughness, misalignment, and curvature changes. Applying retroreflective tape to target surfaces also has the advantage of increasing and maintaining the reflectivity of any target surface. This increases the sensor range and repeatability of measurements. However, proper adhesion of the tape is required, including light sanding, cleaning with isopropyl alcohol, and allowing 24 hours for the adhesive to fully bond.

A linear displacement calibration was performed with a retroreflective tape (Nikkalite 48000 series) applied to a target surface and the flat surface aligned perpendicular to the sensor tip (see Figure 5.2). As shown in Figure 5.6, the superior reflectivity of the tape compared to the original aluminum flat surface increases the sensor range by 9x to 27 mm (every 5th data point shown for clarity).

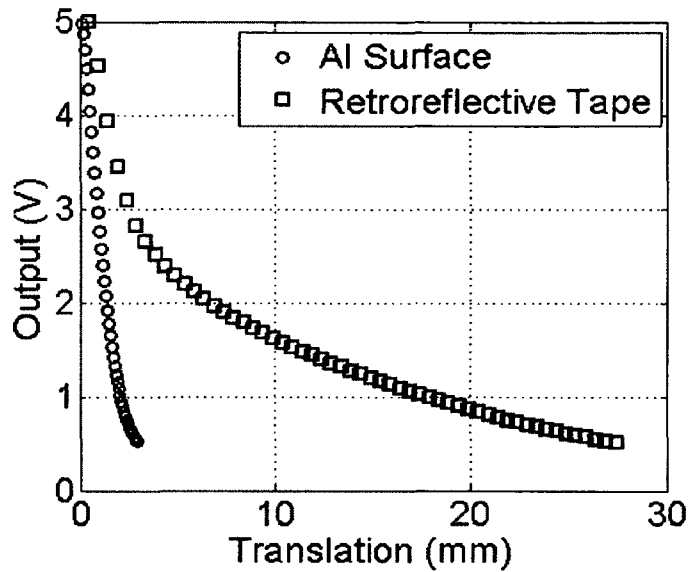


Figure 5.6: Calibration to flat surface with retroreflective tape applied and a with mill-finish Aluminum surface.

Ideally, the retroreflective tape reflects all of the light back to the sensor tip regardless of misalignment, but some scattering does occur. To quantify this, an angular calibration was performed by rotating a flat target surface from a perpendicular starting point (i.e., the experimental setup in Figure 5.4a).

As shown in Figure 5.7, retroreflective tape decreases the sensitivity to misalignment, represented as a percent error from the original displacement reading. Calibrations were performed at various gap lengths to show the misalignment error decreases slightly at longer gap lengths. Note that longer gap lengths allowed larger angular rotations due to less interference with the sensor mount.

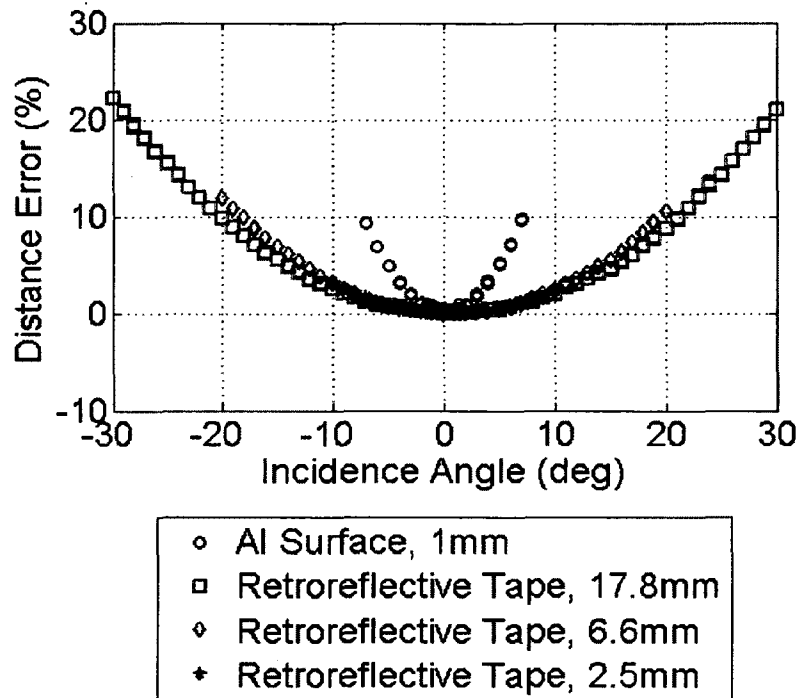


Figure 5.7: Angular effects on flat surface with retroreflective tape applied and a mill-finish Aluminum surface.

5.3 SENSOR IMPLEMENTATION

The fiber optic sensor was implemented in two EMF processes to evaluate the potential for its use in axisymmetric tube welding and flat sheet forming. In both of these processes, a direct comparison with a laser PDV system was performed.

5.3.1 FLAT SHEET FORMING

The fiber optic sensor was implemented in a EM sheet forming process to measure the velocity of 1mm thick, 76x103mm Al 6061-T6 sheets using the Uniform Pressure Actuator (UPA) described Chapter III and IV. Retroreflective tape was applied to the surface of the workpiece and translation calibration (see Figure 5.6) was used.

The fiber optic sensor was incorporated into the clamping fixture to observe the center of the workpiece as it deforms away from the coil. The UPA assembly is shown in Figure 5.8. A HP 54810A oscilloscope with a 500MHz bandwidth and 1GS/s sampling rate captured displacement data. The experiments were conducted on a Maxwell Magneform 7000JA with a rated capacity of 12kJ. EMF processes are controlled by input energy, based on a percentage of the maximum machine energy.

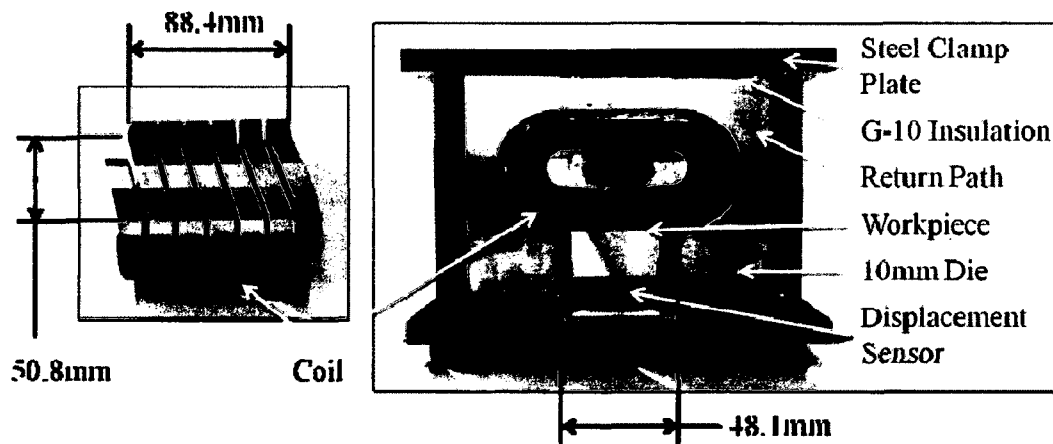


Figure 5.8: Experimental setup for UPA flat sheet forming tests.

Three forming tests were performed at three energy levels of 3.6kJ, 6kJ, and 8.4kJ. An order 50 polynomial (randomly selected) was fit to the retroreflective displacement curve (Figure 5.6) with a least squares method, which provides a continuous curve to differentiate. Polynomial fits of the displacement data fit well during displacement, but some error was observed at low velocities. Velocity was determined from differentiation of this polynomial. For comparison, three tests at the specified energy level were repeated with the PDV system. Velocity results for the three tests at each energy level were averaged and are shown in Figure

5.9. Error bars, representing the range of values for a given energy level, are included.

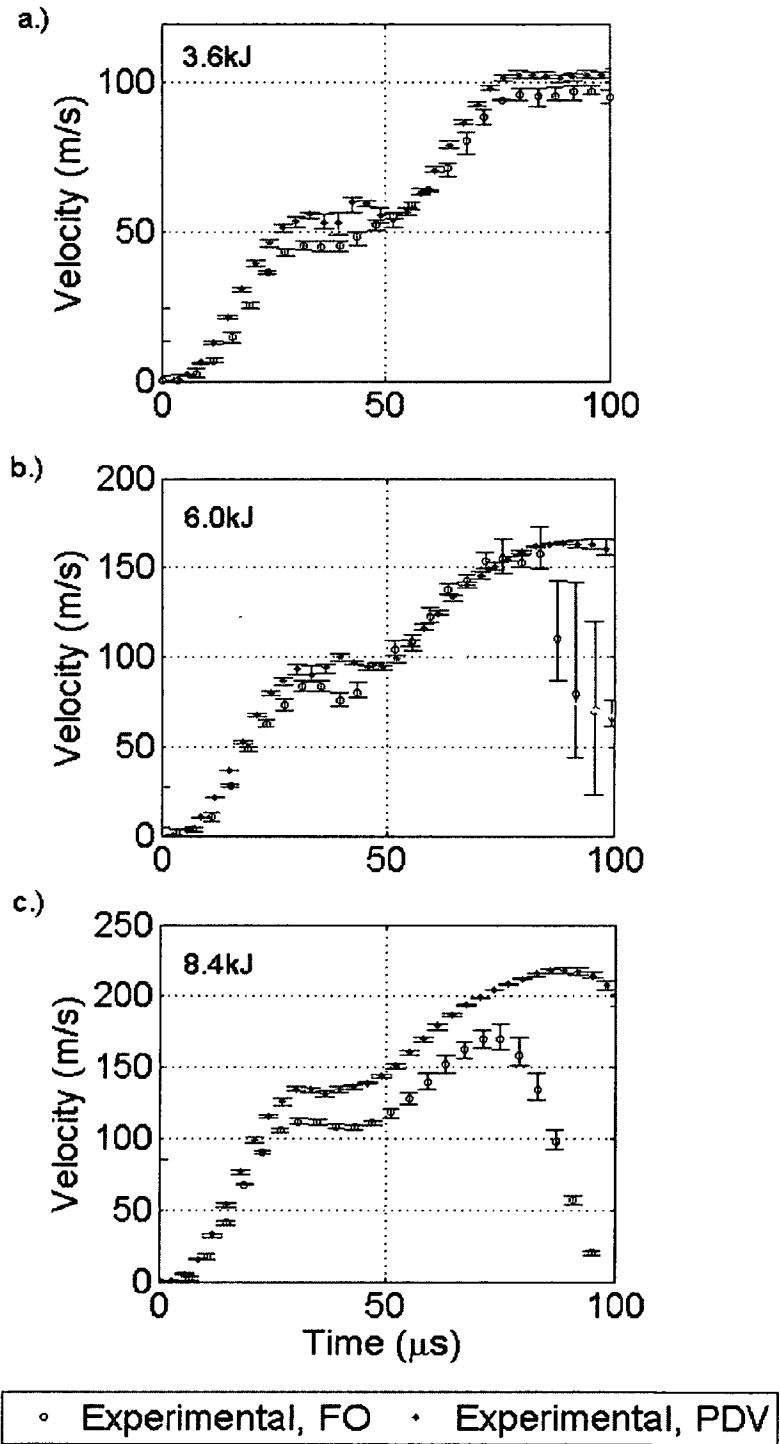


Figure 5.9: Velocity results for 1mm sheet Al 6061-T6 forming at 3.6kJ, 6kJ, and 8.4kJ discharge energies, measured with the fiber optic sensor and the PDV system.

Velocity results are consistent for each experimental run during the initial acceleration. Larger error is observed during the later deceleration for the two higher energy cases, where a combination of the retroreflective tape failing and the workpiece surface deforming caused a loss in reflectance. This loss in reflectance is not distinguishable from actual workpiece displacement with the fiber optic sensor, which results in a lower velocity measurement. For the 8.4kJ case, only the initial slope of the curve is comparable to the PDV data, with lower velocities afterwards. Figure 5.10 shows a photograph of the deformed workpiece from a 6.0kJ discharge, with the location of the sensor indicated.

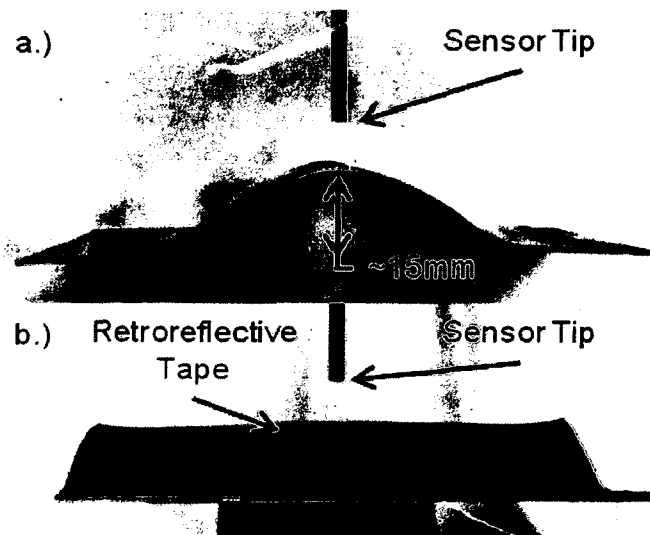


Figure 5.10: a.) Front view and b.) side view of deformed workpiece with a 6.0kJ discharge, with the location of the fiber optic sensor indicated.

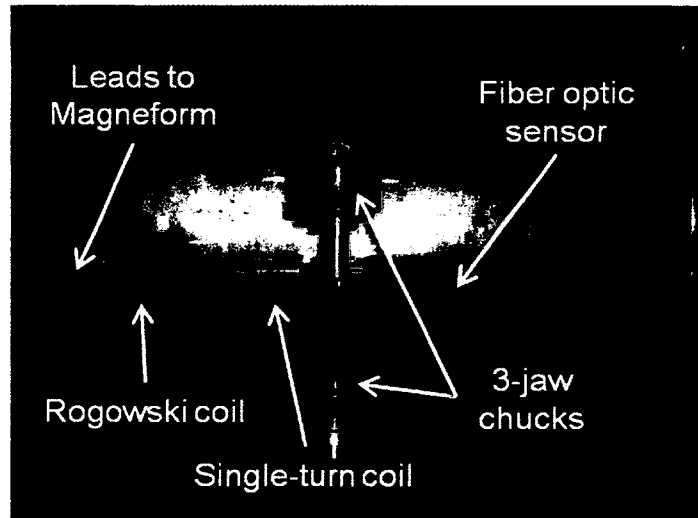
5.3.2 TUBE CRIMPING

To further evaluate the fiber optic sensor in another application, a assembling process for crimping an Aluminum 2024-T3 tube to an Al 6061-T6511 shaft was implemented. The tube outer diameter was 25.4 mm (1") and its wall thickness was 0.89 mm (0.035"). The shafts were machined to a diameter of 21.84 mm

(0.86”), creating a gap equal to one thickness of the tube. The experiments were conducted on the same Maxwell Magneform 7000JA machine.

A single-turn coil was constructed of Cu-Cr-Zr alloy C18150 with an outer diameter of 205.2mm (8in), an inner diameter of 27.4mm (1.04in), and a thickness of 38.1mm (1.5in). A taper angle of 45° on the inner landing of the coil was used to concentrate the magnetic field at the welding location. A 3.175mm (0.125in) radial slot was cut and leads brazed on either side to create a connection to the capacitor bank. (see Figure 5.11a). The sensor was located opposite of this slot by drilling a hole, and was secured with nylon bolts. A cross sectional view of the single turn coil is shown in Figure 5.11b.

a.)



b.)

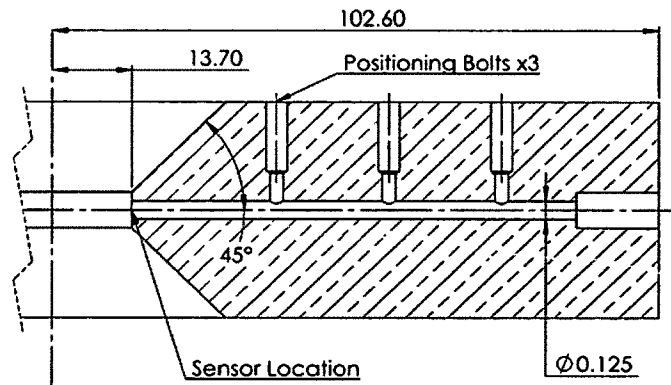


Figure 5.11: a.) Experimental setup for tube/shaft welding in forming box and b.) Cross section view of single turn coil (dimensions are in mm).

As shown in Figure 5.11a, a pair of three jaw chucks was used to hold the tube and shaft in place and aligned during welding. A Powertek CWT 3000B Rogowski coil was implemented on the incoming lead to measure the current through the capacitor bank - coil primary circuit. A Tektronix TDS 2012 oscilloscope with a 100MHz bandwidth and 1GS/s sampling rate captured the displacement and current data.

Three experiments were performed at 7.2, 9.6 and 12kJ discharge energies. For each power level, a translation calibration for this tube material and geometry was performed in the same manner as described in the sensor calibration section. The linear range of the sensor was used to determine the displacement during the deformation, and an order 15 polynomial (randomly selected) was fit to the displacement curve with a least squares method. Polynomial fitting produces a smooth curve to differentiate, and fits the displacement data during deformation. Some error in the fit at low velocities was observed. Velocity is determined from the differentiation of this polynomial.

For comparison, the three sets of experiments were repeated with the PDV system. The PDV probe was positioned in the same hole in the coil to observe the workpiece velocity. Velocity results for the tests are compared in Figure 5.12.

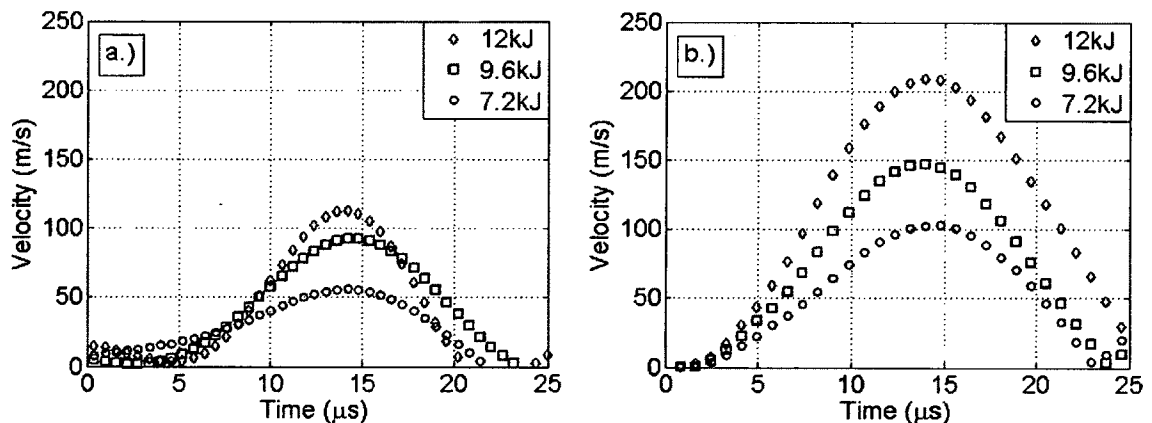


Figure 5.12: Velocity results for 25.4 mm diameter, .89 mm wall, 2024-T3 tubes at various energy levels, measured with a.) the fiber optic sensor and b.) the PDV system.

Considering the PDV measurement to be accurate, the fiber optic sensor shows much greater error in the tube crimping process, in large part due to the increased local deformation relative to the size of the fiber optic sensors light

beam. Figure 5.13 shows a photograph of the deformed workpiece from a 9.6kJ discharge, with the typical location of the sensor indicated.

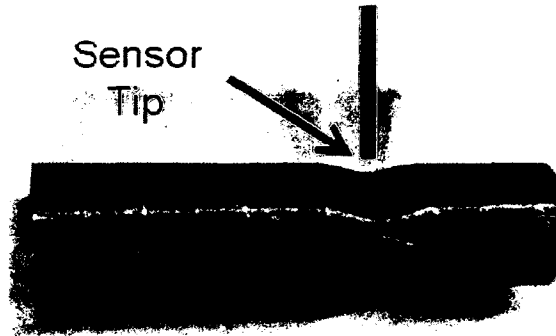


Figure 5.13: Deformed workpiece with a 9.6kJ discharge, with the location of the fiber optic sensor indicated.

Artifacts of the curve fitting are evident in the waviness before and after the launch since the high order polynomial required to fit the transient data did not fit the steady state regions of the displacement data well (i.e. where the velocity is near zero and should have been flat). Additionally, limits bit resolution and signal to noise ratio limit the quality of the original displacement data and the ability to accurately fit data in this region. Since displacement data must be differentiated, original data quality is important for more accurate curve fitting.

5.4 DISCUSSION

5.4.1 RETROREFLECTIVE SURFACE

By implementing retroreflective tape with the fiber optic sensor, significant improvements were achieved. The retroreflective tape was successful in increasing the displacement range by 9x, as well as decreasing the sensor's sensitivity to misalignment. Having a consistent surface reflectivity by applying

the tape to a given surface eliminates the need to calibrate the sensor for each type of surface and improves repeatability.

When deformation increased in the workpiece surface, the retroreflective tape began to fail producing small cracks in the tape surface. This is only a minor effect since the light beam illuminates an area of the tape at a 66° beam angle, so the overall decrease in reflectivity is small. A larger displacement measurement error is expected from the workpiece deformation itself, which decreases the light intensity reflected back to the sensor for a convex surface. A concave surface could have the opposite effect, reflecting more light back to the sensor.

5.4.2 LOCALIZED DEFORMATION

After the 1mm Al 6061-T6 sheet forming experiments, the specimens were placed back in the translation calibration setup to quantify the error in displacement measurement from the tape failing and the surface deforming. The results of the translation calibration are presented as a percent error from the original calibration in Figure 5.14.

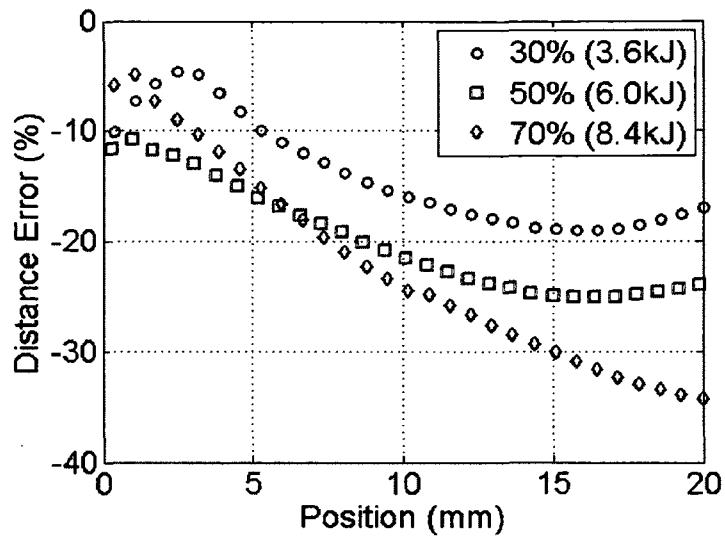


Figure 5.14: Translation calibration with deformed specimen and damaged retroreflective tape.

The combination of the workpiece surface deforming and the retroreflective tape cracking yields a lower effective reflectivity and causes an apparent decrease in distance. As this occurs during deformation of the workpiece, measured velocity would be lower than the actual velocity. This is a limitation of the reflectance-based sensor, so care should be taken to implement the sensor where local deformation (i.e., in the area illuminated by the infrared beam) of the surface is minimal. Additionally, since only static characterization of the sensor is possible before and after the workpiece is deformed, no quantitative error for the measurement of velocity can be determined during the process.

Velocity results are comparable for flat sheet forming for the initial acceleration, until the workpiece surface deformation causes a change in reflectance. This error is larger for tube crimping since the deformation is more localized with the single turn coil. If tube crimping was performed with a multi-turn coil (where a

longer axial section of tube was deformed), sensor performance would be similar to the sheet forming process in the center of the deformation away from the curvature.

Coincidentally, the error in fiber optic sensor data showed slower velocities for both forming processes when compared to PDV measurements. Although the workpiece deformation caused opposite changes in reflected light (i.e., convex for the flat sheet forming versus concave for tube crimping), the sensor observed opposite directions of displacement as well. For example, in the tube crimping experiment, the workpiece displaced away the sensor, so reflected light intensity decreased. However, the concavity slightly increased the reflected light during the displacement, so it appeared the surface has deformed slightly less at a lower velocity.

5.5 SUMMARY

In this chapter, a fiber optic sensor was characterized and implemented in two EMF processes. The sensors response to linear and angular displacement was quantified both with a mill-finish Aluminum surface, and with retroreflective tape. Retroreflective tape was shown to improve the linear range of the sensor by 9x, and to greatly reduce its sensitivity to misalignment. Retroreflective tape also increases repeatability, since a consistent surface reflectivity eliminates the need to recalibrate for each surface condition of various workpieces.

The sensor was implemented in a tube crimping and a sheet forming experiment, where velocity measurements were taken in parallel with PDV. Flat sheet forming

showed the sensor had good accuracy with velocities up to 150m/s accurately for the 6.0kJ case. However, some error was seen at higher velocities, where larger deformations of the workpiece changed the effective reflectivity of the surface.

This effect was larger with tube crimping, where the deformation of the surface was much larger, relative to the sensor diameter. The larger deformation changed the effective reflectivity of the surface, and larger error was observed when compared to PDV velocities.

CHAPTER VI

CONCLUSIONS AND FUTURE WORK

6.1 CONCLUSIONS

6.1.1 UNIFORM PRESSURE ACTUATOR

The analytical model's ability to predict workpiece velocity based on discharge energy level, and workpiece thickness, density, and conductivity was verified experimentally. Also, the analytical model's ability to generate an efficient and robust actuator design for accelerating workpieces electromagnetically was demonstrated. Therefore, the analytical model is a simple and cost effective solution to efficient design of electromagnetic forming actuators and prediction of workpiece velocity for EMF and MPW. Predicting workpiece velocity is a key parameter in MPW, so this modeling helps eliminate the empirical investigation to produce a MPW joint or EMF process.

Major findings from this research are that the magnetic coupling coefficient, k , remains constant for workpiece thickness to skin depth ratios of $\alpha > 0.66$.

Therefore, when $\alpha > 0.66$, the magnetic coupling is only determined from the geometry of the coil and workpiece, and the analytical model's accuracy in predicting workpiece velocity will remain constant for a large range of workpiece thickness and resistivity. Smaller α ratios, e.g., $\alpha = .57$, show decreased magnetic coupling, and therefore, decreased magnetic pressure and workpiece

velocity. The α ratio is a key parameter when adapting an EMF or MPW process to a given workpiece, and this research shows that the previous recommendations of $\alpha > 1.5 - 2.0$ can be lowered. The analytical model will show the same accuracy in predicting workpiece velocity for a larger range of workpiece types, i.e., thinner and more highly resistive workpieces.

The physical interactions of the acceleration process were simplified to solve for workpiece velocity analytically, while still maintaining sufficient accuracy. The predictive power of the model has possibilities for improvement, e.g., determining a coupling coefficient without physical experimentation. Electromagnetic simulations could provide insight into this but is difficult based on its complexity and cost. The simplified modeling presented aims to bridge the gap between experts in pulsed power and electromagnetism, and sheet metal and manufacturing experts. This will allow for increased implementation and leveraging of the advantages of EMF and MPW.

6.1.2 FIBER OPTIC DISPLACEMENT SENSOR

The fiber optic displacement sensor was shown to be a viable solution for workpiece velocity measurement in the EMF and MPW processes. It is attractive for its low cost, ease of implementation, and safety. Characterization was performed to quantify the error in displacement measurements for typical surface effects observed during these forming processes. Through implementing retroreflective tape with the sensor, an increased displacement range of 9x was obtained, as well as decreased sensitivity to misalignment. Repeatability of the sensor is also improved, since a consistent surface reflectivity can be applied to

any target surface. Retroreflective tape is limited by its ability to remain adhered and strain with the target.

Verification of the sensor with high speed deformation was shown with the experiments comparing results to the PDV system. Major findings from this research are that the sensor is an acceptable solution to measuring high velocities, especially if the target is remains relatively flat locally. In the sheet forming process, the sensor was shown to be capable of measuring velocities of at least 150 m/s accurately.

Even with the negative impact of localized deformation, the cost and ease of implementation of the fiber optic sensor are main driving advantages for this velocity measurement technique. In the future, an array of sensors could be implemented at different locations to provide a deformation and velocity profile for various EMF and MPW processes.

6.2 FUTURE WORK

In the future, the predictions and measurements of the workpiece velocity can be used to inform welding tests, where the optimal gap distance between the flyer and stationary workpiece can be determined so that the flyer impacts at maximum velocity. Various energy levels (and therefore impact velocities), impact angles, and workpiece materials will be used to determine which set of parameters produce a weld, and strength of these welds will be observed (e.g., a peel test).

REFERENECEES

- [1] Psyk, V., Risch, D., Kinsey, B.L., Tekkaya, A.E., Kleiner, M., 2011, "Electromagnetic forming - A review". *Journal of Materials Processing*, **211**(5), pp. 787-829.
- [2] Zhang, Y., Babu, S. S., Prothe, C., Blakely, M. Kwasegroch, J., LaHa, M, Daehn, G. S., 2011, "Application Of High Velocity Impact Welding at Varied Different Length Scales," *Journal of Materials Processing Technology*, **211**(5), pp. 944–952.
- [3] PST Products GmbH, 2013 "Applications," <http://www.english.pstproducts.com>, Accessed July 2013.
- [4] Blakely, M., 2008, "Filler Wire is for Wimps," *Fabricating and Metalworking*, <http://www.fabricatingandmetalworking.com/2008/04/filler-wire-is-for-wimps>, Accessed April 2008.
- [5] Zhang, Y., 2010, "Interfacial Microstructure Characterization in Magnetic Pulse Welds," The Ohio State University, WE 701 Lecture.
- [6] Daehn, G., "High Velocity Metal Forming," in *ASM Handbook, Metalworking: Sheet Forming*, Volume 14B, ASM International, 2006, 405-418.
- [7] VanBenthysen, R., Thibaudeau, E., Kinsey, B.L., 2013 "Effect of Specimen Planar Area on Electromagnetic Flanging". *Journal of Manufacturing Processes*, **15**(2), pp. 194-200.
- [8] Watanabe, M.; Kumai, S., 2009, "High-Speed Deformation and Collision Behavior of Pure Aluminum Plates in Magnetic Pulse Welding," *Materials Transactions*, **50**(8), pp. 2035-2042.
- [9] Kamal, M., Daehn, G. S., 2007, "A Uniform Pressure Electromagnetic Actuator For Forming Flat Sheets," *Journal of Manufacturing Science and Engineering*, **129**(2), pp. 369-379.
- [10] ANSYS, 2011, *Multiphysics Solutions Brochure for ANSYS Release 13.0*. ANSYS, Inc.
- [11] Abaqus 6.11 Documentation: Release Notes, 2011, "Time-harmonic eddy current analysis" Dassault Systèmes.

- [12] Kamal, M., 2005, "A Uniform Pressure Electromagnetic Actuator For Forming Flat Sheets," Ph.D. Thesis, The Ohio State University, Columbus.
- [13] Bauer, D., 1967, "Ein neuartiges Messverfahren zur Bestimmung der Kräfte, Arbeiten, Formänderungen, Formänderungsgeschwindigkeiten und Formänderungsfestigkeiten beim Aufweiten zylindrischer Werkstücke durch schnellveränderliche magnetische Felder. Dr.-Ing."-Dissertation, Technische Hochschule Hannover.
- [14] Nopper, R., Niekrawietz, R., Reindl, L., 2010, "Wireless Readout of Passive LC Sensors," *Instrumentation and Measurement, IEEE Transactions*. **59**(9), pp. 2450-2457.
- [15] Jablonski, F., 1976, "Analyse der elektromagnetischen Umformung rohrförmiger Werkstücke. Dr.-Ing." Dissertation, Akademie der Wissenschaften der DDR, Berlin.
- [16] Grover, F., 1946 *Inductance calculations: Working formulas and Tables*, D. Van Nostrand, New York, pp. 70-74.
- [17] White, J. F., 2004, *High frequency techniques: An introduction to RF and microwave engineering*, IEEE Press., Piscataway, N.J, pp. 221, Chap. 7.
- [18] Knight, W., 2012, "Practical Continuous Functions For The Internal Impedance Of Solid Cylindrical Conductors," <http://www.g3ynh.info/zdocs/comps/Zint.pdf>.
- [19] Ogata, K., 2004, *System Dynamics*, 4th ed. Pearson Prentice Hall, New Jersey.
- [20] Al-Hassani, S.T.S., 1975, "Magnetic Pressure Distributions in Sheet Metal Forming". Conference on Electrical Methods of Machining, Forming, and Coating, pp. 1-10.
- [21] Xu, D., Liu, X., Fang, K., Fang, H., 2010 "Calculation Of Electromagnetic Force In Electromagnetic Forming Process Of Metal Sheet". *Journal of Applied Physics*, **107**(12) pp. 124907.
- [22] Hoerner, S. F., 1965, *Fluid-Dynamic Drag*, Published by the Author, pp. 3, Chap. 15.
- [23] Potter, M. C., Wiggert, D. C., 2008, *Schaum's Outline of Fluid Mechanics*. London, pp. 151, Chap. 8.

- [24] Lesuer, D.R., Kay, G.J., LeBlanc, M.M., 2001, "Modeling Large Strain, High Rate Deformation In Metals". Modeling the Performance of Engineering Structural Materials II. Proceedings of a Symposium, pp. 75-86.
- [25] Alloy Physical Properties. <http://www.cadicompany.com/products.phys-34.html>, Cadi Company, Inc., Accessed February 2012.
- [26] Davis, J R. 2001, *Copper and Copper Alloys*, Materials Park, Ohio, pp. 17, 248, 252, 304-305.
- [27] Johnson, J.R., Taber G., Vivek, A., Zhang, Y., Golowin, S., Banik, K., Fenton, G. K., Daehn, G. S., 2008, "Coupling Experiment and Simulation in Electromagnetic Forming Using Photon Doppler Velocimetry," *Steel Research Int.*, **80**(5), pp. 359-365.
- [28] Ohio Manufacturing Institute, 2013, <http://omi.osu.edu>, Accessed July 2013.
- [29] Song, F.M., Zhang, X., Wang Z.R., Yu L.Z., "A study of tube electromagnetic forming", *Journal of Materials Processing Technology*, 151, 2004, 372–375.
- [30] Philips, G. J., 1992, "F-O Displacement Sensors For Dynamic Measurements," *Sensors*, **9**(9), pp. 26-30.

APPENDIX A: ADDITIONAL EQUATIONS

The inductance of a coil, wound in a rectangular form can be found from [16],

$$\begin{aligned}
 L = \frac{0.008}{10^6} n^2 \left(\frac{aa_1}{b} \right) & \left[\frac{1}{2} \frac{b}{a_1} \operatorname{asinh} \left(\frac{a}{b} \right) + \frac{1}{2} \frac{b}{a} \operatorname{asinh} \left(\frac{a_1}{b} \right) \right. & 7.1 \\
 & - \frac{1}{2} \frac{a_1}{b} \operatorname{asinh} \left(\frac{a}{a_1} \right) - \frac{1}{2} \frac{a}{b} \operatorname{asinh} \left(\frac{a_1}{a} \right) + \left[\frac{\pi}{2} - \operatorname{atan} \left(\frac{aa_1}{b^2 \sqrt{1 + \frac{g^2}{b^2}}} \right) \right] \\
 & - \frac{1}{2} \left(1 - \frac{a_1^2}{b^2} \right) \frac{b}{a_1} \operatorname{asinh} \left(\frac{a}{b \sqrt{1 + \frac{a_1^2}{b^2}}} \right) - \frac{1}{2} \left(1 - \frac{a^2}{b^2} \right) \frac{b}{a} \operatorname{asinh} \left(\frac{a_1}{b \sqrt{1 + \frac{a^2}{b^2}}} \right) \\
 & + \frac{1}{3} \frac{b^2}{aa_1} \sqrt{1 + \frac{g^2}{b^2}} \left(1 - \frac{1}{2} \frac{g^2}{b^2} \right) + \frac{1}{3} \frac{b^2}{aa_1} - \frac{1}{3} \frac{b^2}{aa_1} \sqrt{1 + \frac{a^2}{b^2}} \left(1 - \frac{1}{2} \frac{a^2}{b^2} \right) \\
 & \left. - \frac{1}{3} \frac{b^2}{aa_1} \sqrt{1 + \frac{a_1^2}{b^2}} \left(1 - \frac{1}{2} \frac{a_1^2}{b^2} \right) + \frac{1}{6} \frac{b^2}{aa_1} \left(\frac{g^3 - a^3 - a_1^3}{b^2} \right) \right]
 \end{aligned}$$

$$w/ \quad g^2 = a^2 + a_1^2 \quad 7.2$$

where a and a_1 are the cross sectional width and height, requiring $a > a_1$, and b is the length of the coil. In the direction of the length b , there are n turns, and g is diagonal length of the coil cross section [16].

APPENDIX B: MATLAB CODE

ANALYTICAL MODEL

MAIN CODE

```
%% EMF/MPW Research
%% Process Model & Coil Design

%% Initialize

clear all; close all; clc;

%% Parameters
%{
  - List of initial, known, parameters
  - Options for analysis and plotting
%}

% ***** Options *****
opt.aero = 'on'; % Aerodynamic effects
opt.magfieldplot = 'off'; % Plot magnetic fields
opt.legends = 'off'; % Plot legends
opt.bound = 'f2'; % Magnetic field assumption: 'low', 'high',
'f2'
opt.elec_override = 'off'; % Use experimental electrical parameters

% Magnetic Permeability of Free Space
uo = 1.2566370614e-6; % H/m

% ***** Machine Parameters *****
Lm = 0.0721e-06; % H
Rm = 4.38e-3; % Ohm
C = 6*60e-6; % F

% Energy Stored
E = 12e3; % J
E = E*1;

% Initial Charge Voltage
Vco = sqrt(2*E/C);

% ***** Workpiece Dimensions / Properties *****
wrho_d = 2660; %
kg/m^3
wh = 2e-3; % m
wl = 4*.0254; % m
ww = 3*.0254; % m
woff = 6.4e-3; % Workpiece overlap % m
f2 = 0.70;
```



```

% ***** Coil Dimensions / Properties *****
crho_r = 4.8e-8; % ohm*m

% Number of Turns
n = 6;

% Required conductor spacing
b = .003; % m

% Conductor Width
a = (wl-woff*2-(n-1)*b) / n;

% Pitch
p = a+b;

% Coil Dimensions (Defined on mid CS)
ch = 0.020+a; % m
cw = 2*.0254+ch; % m
cl = wl-woff*2-a;

% Coil Outer Dimensions
ch_o = ch+a;
cw_o = cw+a;
cl_o = (cl+p)+a; % Adds half turn on each end for lead attachment

% Conductor Locations (lower)
n1 = woff+(a/2);
n2 = wl-woff-(a/2);
cond_loc = linspace(n1,n2,n);

% ***** Time Constants *****
t_step = 1e-6; % s
t_end = 30e-6; % s

t = 0:t_step:t_end-t_step;
nt = length(t);

% ***** Initial Conditions *****
% Starting Gap
g0 = .003; % m

% ***** Discretization Constants *****
% Length Constants
nx = n*20;
ny = 3;
ni = 500;

%% Coil Resistance
%{
- Analysis of the coil resistance, based on DC resistance with an
effective area due to the skin effect
%}

```

```

% Nominal Frequency
f = 8.9e3; % Hz
w = 2*pi*f;

% Skin Depth
sd = sqrt(2*crho_r/w/uo);

% Effective Area
Aeff = a^2 - ((a/2 - sd)*2)^2;

% Coil Resistance
Rc = crho_r*(2*cl-ch + pi*ch)*n / (Aeff);

% Total Circuit Resistance
R = Rm + Rc;

%% Coil Inductance (Grover) (Implemented)
%{
- Analysis determines the coil inductance based on formula for
inductance
of a single layer coil, on a rectangular form
- Correction for wire insulating space applied
- Assumption: Conductor cross section is round
%}

% Inductance of Single Layer Coil on Rectangular Winding Form
Lc = inductgrover(cw, ch, cl_o, p, a, n);

% Total Circuit Inductance
L = Lm + Lc;

%% Coil Inductance (Kamal) (Not Implemented - For Comparison)
%{
- Analysis of coil inductance based on section of infinitely
long solenoid
%}

Lc3 = (uo*n^2*cw*ch)/(cl_o);

%% Electrical Simulation
%{
- Analysis of the primary current, based on series RLC circuit
- Analytically solution for current. Capacitor voltage is
then solved for by integrating current through the capacitor
%}

if strcmp(opt.elec_override, 'on')
R = 8.6e-3;
L = .418e-06;
end

% Natural frequency
wn = sqrt(1/(L*C));
% Damping Ratio

```

```

z = R/2*sqrt(C/L);
% Damped Natural Frequency
wd = wn*sqrt(1-z^2);

% Circuit current
Ip = Vco*sqrt(C/L)/sqrt(1-z^2) ...
    .* exp(-z*wn.*t) ...
    .* sin(wn*sqrt(1-z^2).*t);

del = wn*z;
Itest = Vco*sqrt(C/L).*exp(-del*t).*sin(wn.*t);

% Capacitor Voltage
V = 1/C .* cumtrapz(t,-Ip) + Vco ;

% Find peak current
[pks,locs] = findpeaks(Ip);

%% Magnetic Pressure & Acceleration

% Workpiece Mass
m = wh*wl*ww*wrho_d;

% x and y locations
x = linspace(0,wl,nx);
y = linspace(0,.020,ny);

% If magnetic field plot is not generated, only determine magnetic
field
% at the workpiece surface
if strcmp(opt.magfieldplot,'off')
ny = 1;
y = 0;
end

% Find x index of workpiece width for mean pressure
for i=1:nx
    if x(i) <= 0
        x_ind_1 = i;
    end
end
for i=1:nx
    if x(i) >= wl
        x_ind_2 = i;
        break;
    end
end

% Preallocate matrices
integ=zeros(ni,ni);
Hx=zeros(ny,nx,nt);
Hy=zeros(ny,nx,nt);
Hx_mean=zeros(1,nt);
Pm=zeros(x_ind_2-x_ind_1+1,nt);
Pm_mean=zeros(1,nt);

```

```

acc=zeros(1,nt);
vel=zeros(1,nt);
pos=zeros(1,nt);
drag_ratio=zeros(1,nt);
mass_ratio=zeros(1,nt);

% Initial sheet position
g = g0;
pos(1) = g;

% For each time step
for q=2:nt
    % For each filament
    for k=1:n
        % For each y position
        for j=1:ny
            if y(j)<=g;
                % For each x position
                for i=1:nx
                    x0 = cond_loc(k);
                    x1 = x(i)-x0-a/2;
                    x2 = x1+a;
                    g = pos(q-1);
                    y3 = y(j);
                    % H Field, x component
                    if strcmp(opt.bound,'low')
                        % Evaluate contribution of each element
                        integ = @(x3,g1) Ip(q) / (2*pi*a^2) * ...
                            ( ...
                                + (g+g1+y3)./((g+g1+y3).^2+(x3).^2) );
                        Hx(j,i,q) = Hx(j,i,q) +
dblquad(integ,x1,x2,0,a,1e3);
                    else
                        % Evaluate contribution of each element
                        integ = @(x3,g1) Ip(q) / (2*pi*a^2) * ...
                            ( (g+g1-y3)./((g+g1-y3).^2+(x3).^2)...
                                + (g+g1+y3)./((g+g1+y3).^2+(x3).^2) );
                        Hx(j,i,q) = Hx(j,i,q) +
dblquad(integ,x1,x2,0,a,1e3);
                    end
                end
            end
        end
    end
end

% Coupling Coefficient
if strcmp(opt.bound,'high')
    f2 = 1;
end

% Mean Magnetic Field
Hx_mean(q) = mean(Hx(1,x_ind_1:x_ind_2,q));
if strcmp(opt.aero,'on')
    % Magnetic pressure
    Pm(:,q) = .5*f2*uo*Hx(1,x_ind_1:x_ind_2,q).^2 - drag_ratio(q);
    % Mean magnetic pressure

```

```

    Pm_mean(q) = mean(Pm(:,q));
    % Workpiece acceleration
    acc(q) = Pm_mean(q)*wl*ww/(m+mass_ratio(q));
else
    % Magnetic pressure
    Pm(:,q) = .5*f2*uo*Hx(1,x_ind_1:x_ind_2,q).^2;
    % Mean magnetic pressure
    Pm_mean(q) = mean(Pm(:,q));
    % Workpiece acceleration
    acc(q) = Pm_mean(q)*wl*ww/(m);
end
% Workpiece velocity
vel(q) = vel(q-1) + trapz([t(q-1),t(q)],[acc(q-1),acc(q)]); % m/s
% Workpiece position
pos(q) = pos(q-1) + trapz([t(q-1),t(q)],[vel(q-1),vel(q)]); % m

% Aerodynamic Drag
M = vel(q)/343;
Cd = 1.13 + .85*(1+.25*M^2);
ro_air = 1.2; % kg/m^3
drag_ratio(q) = ((Cd*.5*ro_air).*vel(q).^2) / Pm_mean(q); % Pa

% Aerodynamic Added mass
mass_ratio(q) = (wl*ww*(pos(q-1)-min(pos))*ro_air) / m;

% Print solution status
clc
fprintf('%%.f of %%.f\n',q,nt)

end

%% Post Processing

Pm_max = max(Pm_mean);
vel_max = max(vel);

% drag_ratio = drag_ratio / Pm_max;
% mass_ratio = mass_ratio / m;

% Output for Abaqus simulation
abq.t = t';
abq.Pm = Pm_mean'./max(Pm_mean);
abq.Pm_max = max(Pm_mean);

% Load Abaqus results
[abq_2mm] = importdata('abaqus_velocity_2mm.txt');
[abq_10mm] = importdata('abaqus_velocity_10mm_2mm.txt');

% Cut Abaqus data to <100% strain
abq_2mm = abq_2mm(1:57,:);
abq_10mm = abq_10mm(1:146,:);

```

SUBFUNCTION

```
function [ Lc ] = inductgrover( a, a1, b, p, d, n )
%INDUCTGROVER Determines inductance of a coil wound on a rectangular
form
% Parameters:
% coil width, coil height, coil length, pitch, conductor width, #
turns

a = a * 100 ; % cm
a1 = a1 * 100 ; % cm
b = b * 100; % cm
p = p * 100 ; % cm
d = d * 100; % cm

g = sqrt(a^2 + a1^2);

Lc = 0.008*n^2*(a*a1/b) * (( ...
    1/2*b/a1*asinh(a/b) ... % 1
    + 1/2*b/a*asinh(a1/b) ... % 2
    - 1/2*(1-a1^2/b^2)*b/a1*asinh(a/b/sqrt(1+a1^2/b^2)) ... % 3
    - 1/2*(1-a^2/b^2) *b/a *asinh(a1/b/sqrt(1+a^2/b^2)) ... % 4
    - 1/2*a1/b*asinh(a/a1) ... % 5
    - 1/2*a/b *asinh(a1/a) ... % 6
    + pi/2 - atan(a*a1/b^2/sqrt(1+g^2/b^2))... % 7
    + 1/3*b^2/a/a1*sqrt(1+g^2/b^2) *(1-1/2*g^2/b^2) ... % 8
    + 1/3*b^2/a/a1 ... % 9
    - 1/3*b^2/a/a1*sqrt(1+a^2/b^2) *(1-1/2*a^2/b^2) ... % 10
    - 1/3*b^2/a/a1*sqrt(1+a1^2/b^2)*(1-1/2*a1^2/b^2) ... % 11
    + 1/6*b/a/a1*((g^3-a^3-a1^3)/b^2) ... % 12
    )) / 1e6; % H

% Correcting for Wire Insulating Space
G = 5/4 - log(2*p/d);
load H.mat
del_Lc = .002*(a+a1)*n*(G+H(n)) / 1e6; % H
Lc = Lc - del_Lc; % H

end
```

EXPERIMENTAL VALIDATION

PDV POST PROCESSING FOR 1MM AL-6061-T6, FORMED AT 6.0KJ

```
%% Initialize

clear all; close all; clc;

%% Read Data (PDV)

% Raw data
data_in1 = dlmread('Raw Data\C1UPA_pdv_50per_1.txt', ',', 5, 0);
data_in2 = dlmread('Raw Data\C2UPA_pdv_50per_1.txt', ',', 5, 0);

% Downsample
downSampleN = 3;
data_in1 = downsample(data_in1,downSampleN);
data_in2 = downsample(data_in2,downSampleN);
fs = 5e9 / downSampleN;

% End Time
t_end = 200e-6;

% Rename data
t = data_in1(:,1);
cur = data_in1(:,2) * 1e5;
pdv = data_in2(:,2);

% Fit sine wave, least squared error fit
downSampleN = 100;
t_end_fmin = 75e-6;
save('sinFitInput','t','cur','t_end_fmin','fs','downSampleN')
res = fminsearch(@sinfit,[8.13e4,175e3,.118,0e-6], ...
    optimset('Display','iter') );
wn = res(1); A = res(2); z = res(3); tOff = res(4);

% Determine Circuit Parameters
t_rise = ((wn/(2*pi))^-1)/4;
t = t + tOff;
cur_fit = heaviside(t) .* A.*sin((t).*wn) .* exp(-z.*wn.*(t));
C = 6*60e-6;
L = 1/(wn^2*C);
R = 2*z*sqrt(L/C);
wd = wn * sqrt(1-z^2);

% Truncate Fit Data
t1 = (find(t>-10e-6,1,'first')); t2 = (find(t>t_end,1,'first'));
t = t(t1:t2); cur = cur(t1:t2);
cur_fit = cur_fit(t1:t2); pdv = pdv(t1:t2);

%% PDV

% Filter parameters
```

```

lowVel = .5; highVel = 200;
cutoff = [lowVel/775e-9/(fs/2),highVel/775e-9/(fs/2)];
[b,a] = butter(1,cutoff);
% Bandpass filter PDV data
pdv_filt = filtfilt(b,a,pdv);

% Window length, samples
wind = 2^11;
% Window length, seconds
windTimeLength = wind/fs;
% Input frequencies to perform STFT
Fin = linspace(lowVel/775e-9,highVel/775e-9,2^9);

% Perform STFT on unfiltered PDV data
[S,F,T] = spectrogram(pdv,wind,wind/2,Fin,fs,'yaxis');
S = 10*log(abs(S)) - max(max(10*log(abs(S))));
T = T + t(1);

% Perform STFT on bandpass filtered PDV data
[S,F,T] = spectrogram(pdv_filt,wind,wind/2,Fin,fs,'yaxis');
S = 10*log(abs(S)) - max(max(10*log(abs(S))));
T = T + t(1);

% Velocity from laser wavelength
V = F*775e-9;

windowPerTEnd = round(((t_end * fs) / wind * 2) - 1);

% Maximum strength frequency selection
vel=zeros(size(S,2),1);
for i=1:size(S,2)
    [C,I] = max(S(:,i));
    vel(i) = F(I)*775e-9;
end

%% Position

% Integrate velocity to determine position
pos = cumtrapz(T,vel)';
pos = pos - pos(find(T>0,1,'first')-1);

% Maximum Velocity
[C,I] = max(vel);
fprintf( ' Peak Velocity           = %.1f (m/s)\n\n',vel(I))
fprintf( ' Pos at Peak Vel           = %.1f (mm)\n\n',pos(I)*1e3)

%% Acceleration

acc = diff(vel)./diff(T');

```